DOT/FAA/TC-22/18

Federal Aviation Administration
William J. Hughes Technical Center
Aviation Research Division
Atlantic City International Airport
New Jersey 08405

A Microwave System for Surface Collection Efficiency Measurements

October 2022

Final report

U.S. Department of Transportation
Federal Aviation Administration

NOTICE

This report is available at the Federal Aviation Administration William J. Hughes Technical Center's Full-Text Technical Reports page: actlibrary.tc.faa.gov in Adobe Acrobat portable document format (PDF).

Form DOT F 1700.7 (8-72) Reproduction of completed page authorized

1. Report No. DOT/FAA/TC-22/18	2. Government Accession No.	3. Recipient's Catalog No.
4. Title and Subtitle A Microwave System for Surface Collection Efficiency Measurements		5. Report Date October 2022 6. Performing Organization Code
7. Author(s) Stephen T. McClain and Brandon J. Herrera		8. Performing Organization Report No.
9. Performing Organization Name and Address Baylor University One Bear Place #97360 Waco, TX 76798		10. Work Unit No. (TRAIS) 11. Contract or Grant No.
12. Sponsoring Agency Name and Address		13. Type of Report and Period Covered Final Report 14. Sponsoring Agency Code
15. Supplementary Notes		

16. Abstract

A microwave system was developed to measure the amount of water collected on a surface of an airfoil relative to the amount of water in a cloud that pass through an equivalent upstream projected area, as well as the ratio of these quantities, which is defined as the surface collection efficiency. Traditional methods for measuring collection efficiency involve attaching blotter paper to an airfoil surface to collect droplets with dye added to the water entering the spray bar system. Following precise spray system actuation, the amount of dye remaining on the blotter paper is measured using a reflectance spectroscopy system. The effort to develop a new microwave system for collection efficiency measurements included: 1) construction of two single-waveguide models and one partial airfoil model with multiple microwave waveguides and a multiplexing system, 2) construction of a spray system for the Liquid Film and Cloud Chamber (LFACT) at the Baylor University with fast pneumatic actuation, and 3) testing of the microwave sensing system in the LFACT. The feasibility and operating physics of the microwave elements was verified, and multiple methods for using the system in a larger icing wind tunnel were explored. The spray bar system demonstrated adequate cloud actuation times for the most useful measurement approach. However, the clouds generated in the LFACT were found to be non-uniform. Methods were explored to account for the cloud non-uniformity in the LFACT for future microwave- sensor collection efficiency investigations. A provisional patent (Application # 63/239,207) has been filed for the flexible printed circuit board (PCB) and microwave sensing approach for liquid film thickness measurements with the title “A Microwave System for Detection and Characterization of Materials Interacting with Aircraft and Airfoil Surfaces.”

17. Key Words Icing, Collection Efficiency, Microwave, Sensor	18. Distribution Statement This document is available to the U.S. public through the National Technical Information Service (NTIS), Springfield, Virginia 22161. This document is also available from the Federal Aviation Administration William J. Hughes Technical Center at actlibrary.tc.faa.gov.		
19. Security Classif. (of this report) Unclassified	20. Security Classif. (of this page) Unclassified	21. No. of Pages 65	19. Security Classif. (of this report) Unclassified

Contents

Figures

Tables

Acronyms

Acronym	Definition
ABS	Acrylonitrile butadiene styrene
AOA	Angle of attack
CFD	Computational Fluid Dynamics
FAA	Federal Aviation Administration
IF	Intermediate frequency
IRT	Icing Research Tunnel at NASA Glenn Research Center
LFACT	Liquid Film and Cloud Tunnel
LWC	Liquid Water Content (gm/m^3)
MVD	Median Volumetric Diameter (50%)
NASA	National Aeronautics and Space Administration
PCB	Printed circuit board
RF	Radio frequency
SLD	Supercooled Large Drop
VNA	Vector Network Analyzer

Executive summary

The local rate of water collection on an airfoil or aircraft surface is an important aspect of in-flight ice accretion. As a cloud flows around an airfoil or wing surface, not all droplets will impinge the airfoil. Smaller droplets tend to follow the flow around the airfoil, while larger droplets with more mass and inertia will impact the surface. Computational codes used to predict ice accretion shapes that form on aircraft surfaces during flight must accurately predict the amount of water that impacts the wing surface. The ratio of the amount of water that impinges a surface to the amount of water passing through an equivalent upstream area of the cloud is typically referred to as the collection efficiency.

Because collection efficiency is a time-averaged concept that relates to the impingement of discrete drops hitting the airfoil surface, measurements of collection efficiency have proven to be challenging. The measurements that are currently available for ice-accretion code validation and cloud physics investigations are based on a blotter-paper technique developed in the 1990s where models with paper attached to the surface were exposed dye-laden clouds. A laser scanning system was used to determine the amount of dye remaining on the paper and its variation along the model surface after the paper was removed from the model and allowed to dry.

For the current study, a microwave-based approach was developed as a new method for measuring collection efficiency or alternatively, the amount of water that collects on the airfoil models. Microwave signals launched along surface waveguides are affected by the water that is present on the surface. Water molecules are polar and interact in multiple ways with the electromagnetic fields that are excited at microwave frequencies. Further, the interactions are a function of the amount of water present on the surface. The water-microwave interaction measurement approach employed in this study was the waveguide phase delay which was measured using a vector network analyzer.

Three sensor models were developed. Two sensors with a single waveguide and exhibiting specific aerodynamic shapes were constructed to investigate sensor operation and repeatability. A third sensor model was developed using multiple waveguides and a multiplexing or switching system to use one vector network analyzer for each of the waveguides. The sensor models were constructed using three-dimensionally printed structures, and the sensors were created using flexible circuit boards glued to surfaces of the printed structures. The use of thin, flexible circuit boards epoxied to the surface minimized the aerodynamic impact of the sensors on the flow.

The Liquid Film and Cloud Tunnel (LFACT) at Baylor University was modified during this study. A new spray-bar system was constructed using electronic pressure regulators for fast

cloud creation. A specialized liquid water content probe was used to characterize the clouds created in the LFACT. The cloud creation was determined to be sufficiently fast for the measurements, but the clouds were not uniform over the cross-sectional area of the wind tunnel.

Each of the three sensor models were exposed to various clouds generated in the LFACT. Additionally, a calibration stand was constructed to validate the microwave water measurements made using the multi-waveguide sensor. The findings using the LFACT are summarized as:

1) The operating principle and physics of the wire response to the presence of water was demonstrated using the single-waveguide models. The sensors were sensitive to the accumulation of water during a cloud exposure. When exposed to a passing cloud, the permittivity increased asymptotically to a value determined by a steady-state film thickness.

2) The sensitivity of the single-waveguides to the model angle of attack was demonstrated. However, the repeatability and angle of attack sensitivity investigations were affected by the repeatability of the wind tunnel to establish the clouds quickly compared to the linearity region of the sensors.

3) The multi-waveguide sensor operation and multiplexing system was demonstrated and refined.

4) The blotter cloth approach to characterizing the water collection was found to be most repeatable when using the multi-waveguide sensor. The approach is like the approach of Papadakis et al. (Papadakis, et al., 2007) for collecting water on the surface of the airfoil, but the measurements are essentially immediate, and the cloth or paper can be reused between tests if sufficient time is provided for the blotting-media to dry.

Because of the cloud non-uniformity, two alternative approaches to validating the multi-waveguide sensor using the measured liquid water content variations were explored. Each approach will require inferences about collection efficiency based on the amount of mass or the thickness of water that collects at each waveguide location. Continued efforts following the completion of the current study will focus on 1) modification of collection efficiency predictions based on the measured cloud non-uniformity and 2) numerical simulation of non-uniform clouds using multiple injections with different numbers of droplets.

1 Introduction

The objective of the research activities in this study was to develop a microwave system to measure the amount of water collected on an airfoil surface relative to the amount of water in a cloud that should impinge an equivalent projected area, as well as the ratio of these quantities. This ratio is defined as the surface collection efficiency. The collection efficiency is an important parameter that ice accretion codes must capture to predict the ice shapes that form on aircraft surfaces during atmospheric icing conditions. Most available collection efficiency information was based on ink and blotter paper measurements that were made in the 1990s and early 2000s.

2 Technical background

In this section, a description of airfoil surface collection efficiency and its importance in ice-accretion simulation tools is provided. Additionally, the basics of microwave fields and their interactions with water molecules is presented. Finally, the working theory of how a new sensing approach and data reduction approach was used to measure water collecting on an airfoil surface is discussed.

2.1 Definition of collection efficiency

The local rate of water collection on an airfoil or aircraft surface is an important aspect of aircraft in-flight ice accretion. As an airstream with water droplets, or a cloud, flows around an airfoil, not all droplets impinge the airfoil. When the flow moves around the airfoil, as shown in Figure 1, smaller droplets move with the flow around the airfoil because of the local drag forces on the droplets. However, larger droplets may have sufficient inertia to resist abrupt changes in the flow direction and impinge the airfoil. The local rate of water collection is further complicated by the fact that as the larger droplets impinge the airfoil or aircraft surface, they may splash, and part of the mass of the droplet is entrained back into the freestream flow.

Based on the droplet interactions shown in Figure 1, aircraft icing analyses typically employ a parameter called the collection efficiency, β, to determine the amount of water that impinges an airfoil or aircraft surface. In icing situations with an evenly distributed cloud, the collection efficiency is defined as the rate of water accumulation on an area of the surface relative to the rate that water passes through an equivalent projected area (dA_f) upstream of the flow effects of the airfoil:

$$\beta = \frac{\dot{m}_{Sa}}{LWC \cdot V \cdot dA_f} \tag{1}$$

Where LWC is the liquid water content of the cloud (gm/m^3), V is the air velocity relative to the airfoil, and $\dot{m}_{Sa}$ is the rate of water mass accumulated over the incremental area $dA_f = dS_a \cdot w$, where w is the span of the airfoil.

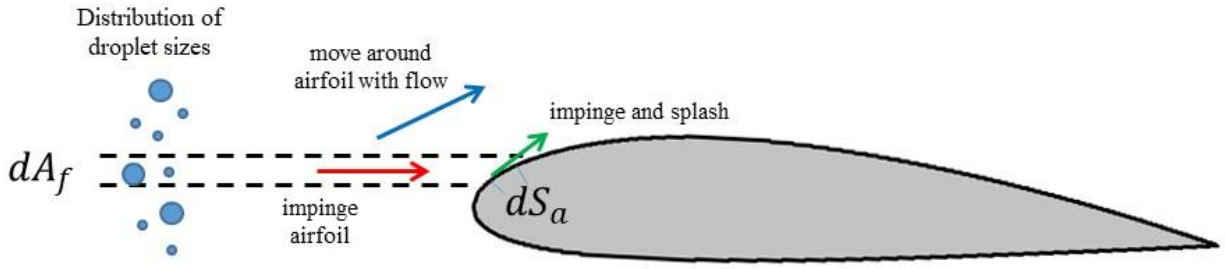

Figure 1. Droplets impinging and airfoil

In ice accretion codes such as LEWICE (Wright, 2008), correctly predicting the local rate of water collection on a surface is crucial. Most ice-accretion codes are based on a Messinger (1953) style approach, and determining the rate of mass addition into an incremental area along the surface of an airfoil or aircraft is the first step in determining the rate at which ice will accrete on the surface. The thermodynamics of the solidification process can only be analyzed after the amount of water entering a control volume along a surface is determined.

Historically, two approaches have been used to predict the local collection efficiency rates. The first approach uses surface geometric arguments after calculating the stagnation-point collection efficiency, β_0, of Langmuir and Blodgett (1946), based on the flow and the median volumetric diameter (MVD). The second and most common approach, and which is used in LEWICE, is to separate the cloud droplet size distribution into a number of groups, or bins, that contain a range of droplet sizes that should behave similarly as the flow moves around the airfoil. Particle trajectory calculations are performed for the droplets of each bin to determine the collection rate along the surface for each bin. The collection efficiency for each bin is volumetrically averaged based on the original droplet size distribution to determine the overall local collection efficiency (Wright, 2008).

2.2 Past measurement methods for collection efficiency

Because of its importance in ice-accretion prediction codes, measuring the local collection efficiency along an airfoil or ice shape surface has been the focus of prior investigations, the most significant of which is Papadakis et al. (2007). To measure the collection efficiency along different airfoils and artificial ice shapes, Papadakis et al. attached blotter paper to the surface and added blue dye to the water entering the spray bar system. Following actuation of a precise

solenoid-valve controlled spray system, the amount of dye on the blotter paper was measured using a reflectance spectroscopy system. The system was implemented in both the Goodrich Icing Tunnel and the National Aeronautics and Space Administration (NASA) Glenn's Icing Research Tunnel (IRT).

While the measurements of Papadakis et al. (2007) provided substantial validation data for collection efficiency predictions in icing codes, the blotter paper approach is very tedious and difficult to implement. Additionally, 1) issues regarding the splashing measurements inferred from the Papadakis et al. data are not universally accepted, 2) collection efficiency data are needed for airfoils exposed to supercooled large drops (SLD), Appendix O conditions (Airplane and engine certification requirements in supercooled large drop, mixed phase, and ice crystal icing conditions, 2015) and clouds with bimodal distributions, and 3) collection efficiency predictions have not been validated on three-dimensional wings and complex (multi-element) airfoils.

2.3 Microwave measurement theory

A new approach was proposed to measure local collection efficiencies more quickly and easily based on microwave spectroscopy. Electromagnetic waves are influenced by two material properties, permittivity, and permeability which control signal loss and velocity of propagation.

Figure 2 demonstrates how water molecules interact with oscillating electro-magnetic fields. As an alternating current signal propagates through a wire, the magnetic fields change in the region surrounding the wire. Because of the orientation of the hydrogen and oxygen atoms, water molecules are polar. When water molecules are in the magnetic field region, they move to align the polarity of the water molecules with the direction of the magnetic fields. The polarity of water contributes to a nearly two-order of magnitude increase in its permittivity over that of free space and non-polar molecules.

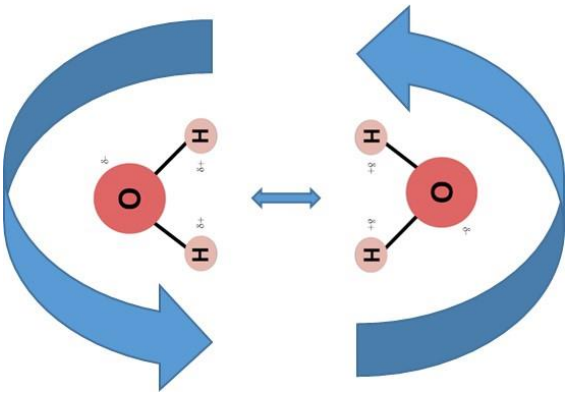

Figure 2. Response of water molecules in oscillating magnetic fields

This large difference facilitates microwave sensing of water in various mixtures and forms. Many measurement methods exist to detect changes in permittivity, but this work focuses on the phase response of coupled transmission lines. The coupled transmission line approach is demonstrated in Figure 3, which shows two interacting wires. When air is above the two interacting transmission lines embedded in a low-permittivity circuit board, the air above the board does not significantly affect the interacting magnetic fields. However, as demonstrated in Figure 3(b), when water molecules are present, the polar molecules interact with the fields by absorbing energy and by potentially creating a difference in the propagation time of a signal through each wire.

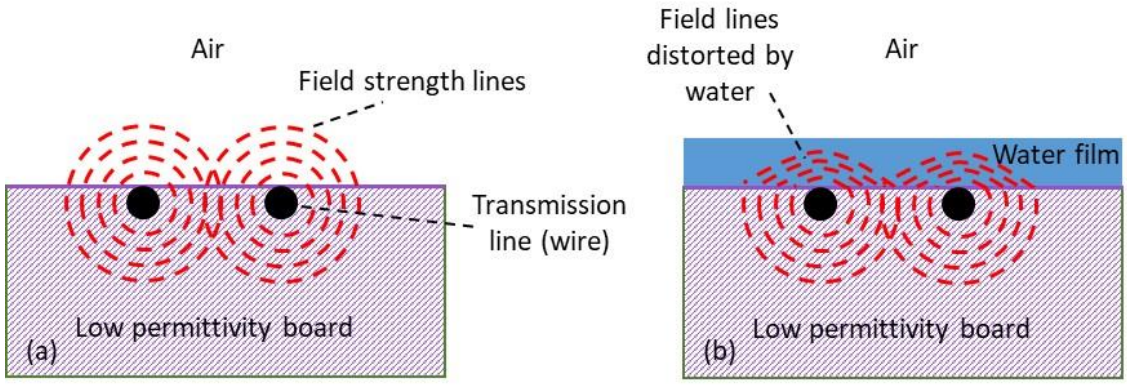

Figure 3. Interaction of water with magnetic fields created at microwave frequencies

2.4 Microwave characteristics of water and mixed species

For the purposes of theory demonstration, permittivity is represented as a scalar dimensionless number which is relative to that of a vacuum. The relative permittivity of water (ε_{water}) varies over frequency (f) and temperature (T) and follows a Debye relaxation model for polar molecules shown in Equation 2 (Hasted, 1973).

$$\varepsilon_{water}(f,T) = 4.9 + \frac{\varepsilon_{w0}(T) - 4.9}{1 + \left(\frac{f}{f_0(T)}\right)^2} \tag{2}$$

In Equation 2, ε_{w0} is water's static dielectric constant, and f_0 is its relaxation frequency, both functions of temperature. Between 0°C and 20°C the relaxation frequency is 9.0 GHz and 17.2 GHz respectively which designates an upper bound for the frequencies of practical sensing. Frequencies above the relaxation frequency exhibit much lower permittivity, which drastically degrades electromagnetic sensitivity. At 10 GHz water's permittivity varies between 42.1 and 60.9 as temperature is increased from 0°C to 20°C, thus, significant temperature variations would require compensation.

The relative permittivity of air (ε_{air}) is dependent on pressure (P), temperature (T), and its water vapor density (ρ_w) from Equation 3, where A, B, and C are constants (Nyfors & Vainikainen, 1989).

$$\varepsilon_{air}(P, T, \rho_w) = 1 + A\frac{P}{T} + B\frac{\rho_w}{T} + C\rho_w \tag{3}$$

The relative permittivity of air can be represented as a constant over frequency and is much lower than liquid water. At 0°C the relative permittivity of air varies between 1.00056 and 1.00062 depending on humidity. Changes in humidity make a small and often negligible impact in microwave sensing compared to the liquid water content effects.

For mixtures and non-homogeneous materials, ***effective permittivity*** is used to describe the measurement environment. The effective permittivity is defined as the equivalent permittivity which a solid homogeneous material would produce the same electromagnetic response. For example, the effective permittivity of the cloud mixture (ε_{cloud}) can be modeled by the Maxwell-Garnett formula in Equation 4 (Levy & Stroud, 1997), which essentially averages the permittivities of air and water based on volume of each substance present.

$$\varepsilon_{cloud}(\varepsilon_{water}, \varepsilon_{air}, \varphi_w) = \varepsilon_{air}\frac{2\varphi_w(\varepsilon_{water} - \varepsilon_{air}) + \varepsilon_{water} + 2\varepsilon_{air}}{\varepsilon_{water} + 2\varepsilon_{air} + \varphi_w(\varepsilon_{air} - \varepsilon_{water})} \tag{4}$$

This approximation is valid for spherical water droplets given the volume fraction of water in the mixture (φ_w). For a very wet cloud that is 0.5% water by volume at 0°C, the relative permittivity is approximately 1.015, which is only 1.5% greater than that of air. This small difference in the cloud permittivity is more challenging to resolve and presents a negligible impact in the presence of liquid water. Planar microwave sensors, which are used in the present work, are most sensitive to materials near their surface. Thus, the accumulation of millimeter scale liquid drops, beads, and films on the sensor face are the dominating factor over the atomized cloud.

2.5 Phase delay measurements using VNA

The distortion of the electromagnetic fields demonstrated in Figure 3 can be measured using two approaches. The first method employs a pattern of wires or a cavity that resonates at a set frequency based on the surrounding effective permittivity. As the surrounding permittivity changes based on the volume averaging expression of Equation 4, the resonant frequency of the system is measured to determine the amount of water present. This is mechanically analogous to measuring the pitch of a tuning fork submerged in water.

The second approach is a phase delay approach. As a signal is launched into to the wires, the high polarity of the water resists the changes in fields, which slows the signal down. The unit of permittivity is capacitance per meter. The units imply that the larger the permittivity, the more time it takes to figuratively charge the capacitor. This change in signal velocity results in a phase-angle shift between the signal launched on the wire and the signal measured coming out of the wire. The amount of phase shift is directly correlated to effective permittivity which is close to a volumetric average depending on the water thickness. Once the relationship between volumetric average permittivity and phase shift is known, equations 2 to 4 are used to determine the amount of water present. The theory of permittivity measurements using microwave sensing approaches is mature and is covered in multiple chapters of the textbook by Nyfors and Vainikainen (1989).

The phase delay approach is the process of characterizing the delay of an electromagnetic signal as it propagates down a dispersive microstrip transmission line. As the transmission line is exposed to materials incident on the airfoil, the signal exhibits a short delay due to its now increased electrical energy storage capacity. This increase in propagation time for the signal is dependent on the effective permittivity of the material surrounding the line. The larger the effective permittivity, the larger the delay as electromagnetic propagation time is a function of the square root of its permittivity.

The delay caused by the change in effective permittivity can either be measured in the time domain with a pulsed excitation or in the frequency domain with sinusoidal excitation. Since the length of the transmission line is known, the measurable increase in delay is manifested by a phase shift between the launched wave and the measured output wave. A Vector Network Analyzer (VNA) is typically required to perform measurements of the phase shift at many frequencies. A VNA produces a sine wave at a specific frequency at its output port then measures the sine wave's changed amplitude and phase at its input port. The frequency is increased, and the measurement is repeated. The phase of each frequency measurement is indiscriminate so the data must be unwrapped where each subsequent frequency point has integer multiples of 2π added to maintain continuity. If the true phase delay shifts by more than 2π between two measurement points, there is a phase discontinuity and the unwrapped data is inaccurate. The VNA's frequency step size must be small enough for this to not occur.

A simple transmission line on a printed circuit board is shown in Figure 4. In Figure 4(a), the transmission line, also known as a waveguide or wire, and PCB are shown with a ruler to demonstrate the size of the sensing length. The transmission line and vector network analyzer are

shown in Figure 4(b), and the transmission line with water beads interacting with the wire are shown in Figure 4(c).

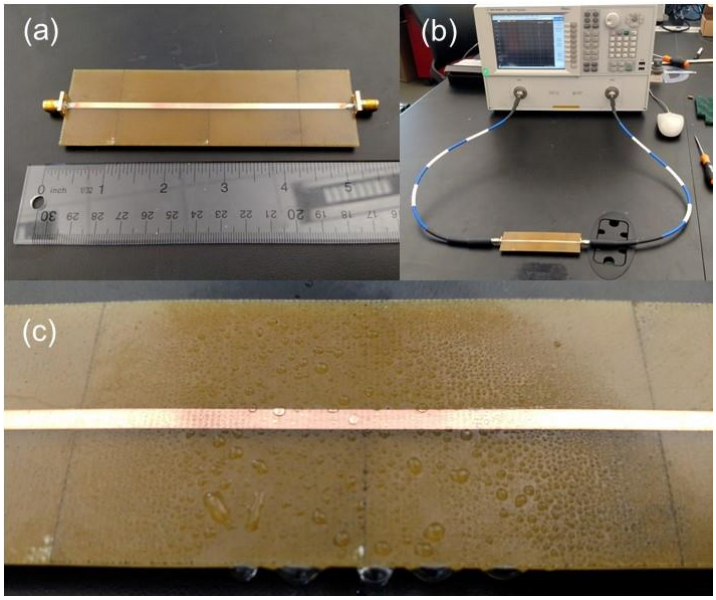

Figure 4. Simple transmission line with vector network analyzer
(a) Geometry of transmission line (wire), (b) Vector network analyzer and transmission line, (c) Transmission line and wire with water on surface of printed circuit board

Figure 5 demonstrates an example of the relative phase shift as a function of the signal frequency of the single sensor interacting with air and water at discrete times. As noted in Figure 5, the presence of the water near the transmission line causes a change in the phase at each frequency where the relative phase of the output signal is essentially linear with respect to the frequency of measurement. An Anritsu MS46122A was used set to transmission mode with maximum Radio Frequency (RF) and Intermediate Frequency (IF) bandwidth to capture the largest phase change within the shortest amount of time. A 40 Megahertz (MHz) frequency step size was selected experimentally to be the largest step size to not produce ambiguous phase discontinuities when exposed to water.

In Figure 5, the phase shift as a function of frequency is essentially linear for the linear sensors used on the models, and the slope of the phase shift is a parameter that is characterized in time as water accumulates in the sensor detection volume. As water interacts with the sensor, the phase shift decreases with the increased relative permittivity of the volume. The difference in the derivate of the phase shift versus frequency from the dry state to the wet state becomes the change in propagation delay due to water (Δt_{pd}) as defined in Equation 5.

$$\Delta t_{pd} = t_{pdDRY} - t_{pdWET} = \left.\frac{d\phi}{df}\right|_{dry} - \left.\frac{d\phi}{df}\right|_{wet} \quad (5)$$

Noting that the phase shift has units of radians and that the frequency has units of radians/second, the dimension of the propagation delay is time.

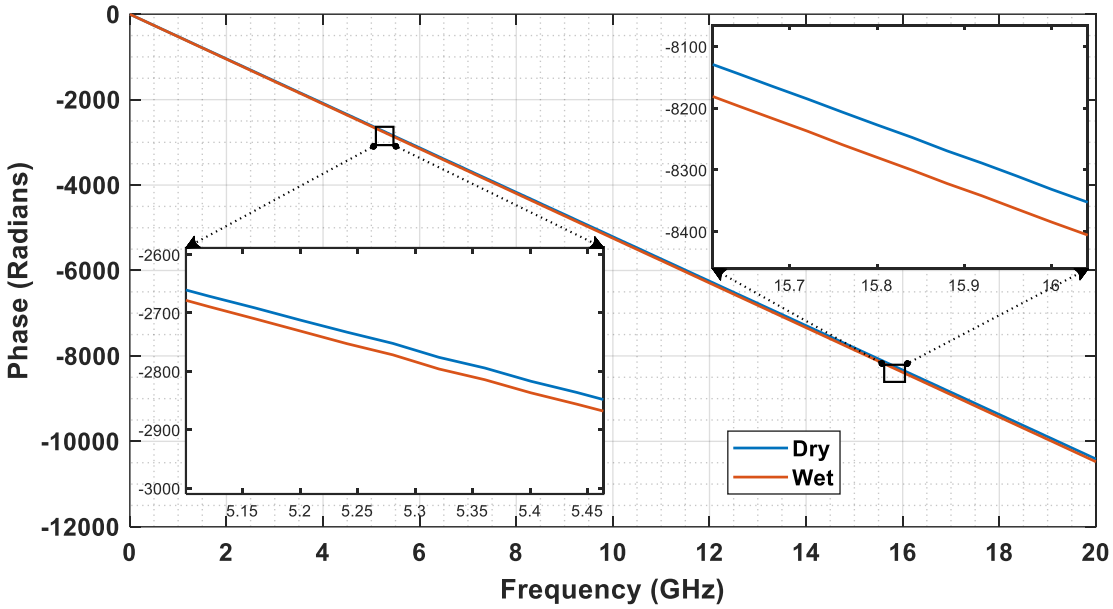

Figure 5. Typical phase response of a single wire sensor dry and during or after water exposure

Figure 6 presents a transient measurement of propagation delay of single transmission-line (waveguide) sensor when exposed to a cloud and beginning with a dry state. To create Figure 6, the VNA data is saved following the conclusion of its measurement cycle through the range of microwave frequencies. The propagation delay is calculated using Equation 5 using the slope of the phase shift with respect to frequency. The time of acquisition becomes the x-axis in Figure 6 and is limited by the speed of the VNA. The different curves of Figure 6 represent a repeatability trial for the single-sensor. That is, each curve in Figure 6 represents a single measurement from the sensor when exposed to the same cloud conditions. Figure 6 demonstrates that all the tests exhibit a region where the propagation delay is essentially linear, which is followed by an unsteady period with non-linear trend. As time progresses, the trend asymptotes to a standing-film thickness measurement. The initial linear region is caused by the initial droplets collecting in the sensing region near the waveguide.

At some point, sufficient water collects or a large drop impacts the sensing surface, and a bead large enough to run along the surface under the pressure and shear forces present forms. In Figure 6, the unsteadiness is caused by the movement or runback of beads of water out of the measurement volume of the sensor. Consequently, the linear region, in which the liquid film has

not fully formed, and beads have not begun to run, is the desired measurement time when the sensors are used for collection efficiency measurements.

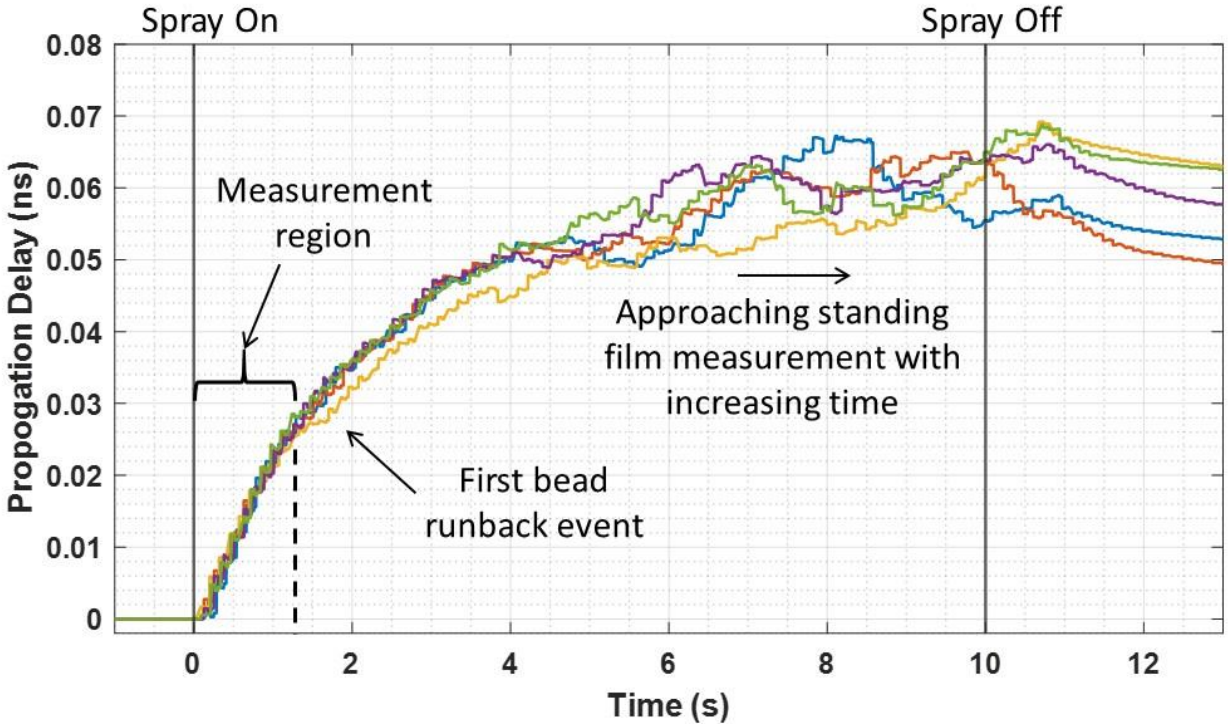

Figure 6. Transient propagation delay response of a single wire during repeated tests

Over the measurement region identified in Figure 6, two approaches exist for measuring the rate of water accumulation near a waveguide. When the VNA is sampled at a sufficiently high rate for one waveguide, a regression analysis may be performed to obtain a continuous, functional representation of the propagation delay as a function of time. The slope of the propagation delay or the associated rate of increase in relative permittivity as a function of time can be determined and reported as propagation delay per unit time or permittivity per second. The rate of permittivity change is then used to determine the rate of water capture on the surface.

If multiple wires are sampled or if the VNA cannot sample an individual waveguide fast enough to create a sufficient number of points for regression analysis and generation of a representative continuous function, then discrete measurements of the phase delay and permittivity before the spray start and at the end of the measurement region are used to determine the discrete change in the permittivity during a test. The discrete measurement approach results in measurements of the change in propagation delay or the change in permittivity for multiple waveguides. The change in permittivity relates to discrete changes in water interacting with each waveguide during a spray event.

2.6 Implementation approach

Based on the understanding of how the transmission-line sensors respond to a transient cloud passing with droplets impinging the surface, the conceptual approach to a system for collection efficiency measurements is depicted in Figure 7. Multiple transmission lines, or waveguides, were aligned in the spanwise direction on a flexible PCB, as shown in Figure 7(a). Sixteen spanwise waveguides were constructed around the leading edge of the airfoil.

The locations of the waveguides along the surface are shown in Figure 7(b) in the projected x-y plane of the airfoil. By being wrapped along the surface of the airfoil with the axial direction of the wires or waveguides in the airfoil spanwise direction, each individual waveguide results in the measurement of the amount of water collecting on the airfoil surface at the waveguide's surface distance from the leading edge. If the cloud has spatially consistent properties, the resulting measurements provide values that are averaged in the spanwise direction, *z*. This measurement approach is consistent with traditional collection efficiency prediction methods employed in ice accretion solvers such as LEWICE (Wright, 2008).

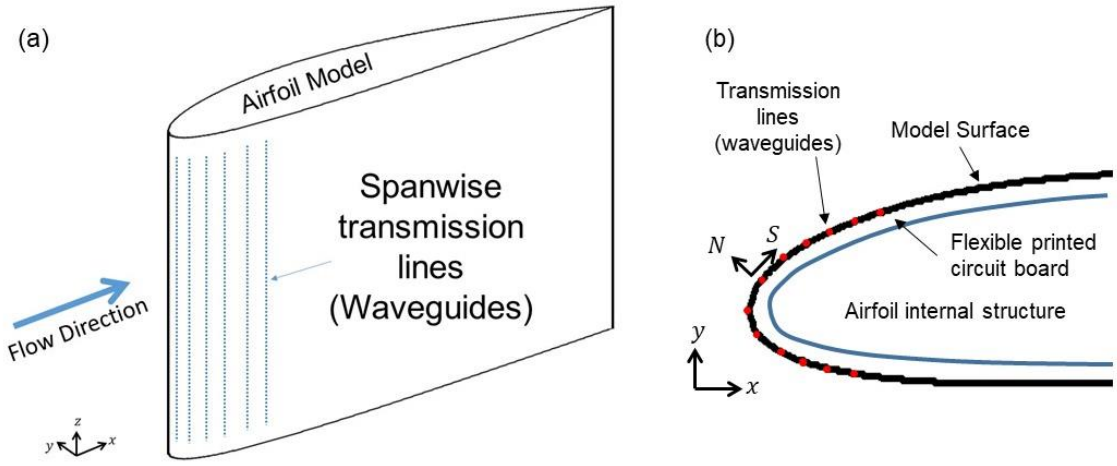

Figure 7. Conceptual implementation of sensors for collection efficiency measurements (a) Three dimensional view and (b) x-y projected view of leading edge

For the system implementation in this study, multiple VNAs were not used to simultaneously determine the properties of each wire. Because of the multiple lines required to measure the collection efficiency along the streamwise surface direction, a multiplexing or scanning system was needed to perform microwave measurements along the surface of the airfoil.

2.7 Objectives

The objectives of this study were to develop, calibrate, and validate a microwave system to measure the amount of water collected on a surface of an airfoil based on the planar phase delay approach. The total amount of water relative to the amount of water in a cloud that should impinge an equivalent projected area, which is defined as the surface collection efficiency, would also be measured using the system.

Equations 2 to 4 describe how water collecting on the surface will change the propagation delay of the sensors. However, a calibration system was created to verify the theory, measure the permittivity of the flexible circuit, and account for any interference between the individual wires when the system is operating with the multiplexing system.

Because of the need to validate the system, the Liquid Film and Cloud Tunnel (LFACT) at Baylor University was modified as part of this study. To expose the sensors to abrupt cloud condition as represented in Figure 6, a fast-actuating spray system was designed and constructed for the LFACT. The precise control of the spray bar system is required because the surface must be exposed to a cloud for a fixed time allowing water to collect on the surface in sufficient volume to be measured but not runback along the surface.

Finally, to perform validations of the sensor performance, the uniformity of clouds generated in the LFACT were to be characterized. Equation 1 is based on having evenly distributed droplets within the clouds generated for validation of the sensor models. If the clouds generated in the LFACT exhibit significant cloud spatial variations within the tunnel cross section, methods outside the simulation approach of LEWICE must be used to validate the sensor operation.

3 Single sensor models

Two single transmission line models, or referred to now as single waveguide models, were created to explore operational characteristics, to explore best VNA operational approaches, and to investigate sensing methodology when using transient cloud or spray bar operation. The single waveguide models were also constructed as a secondary calibration approach when interacting with wind tunnel clouds. That is, the two geometries selected were expected to exhibit specific collection efficiency behaviors relative to each other. As such, the sensors were created to exhibit a desired relative sensor response to one another.

The two geometries selected are shown in Figure 8. In Figure 8(a), the design geometry of the Pi sensor is depicted. Figure 9(a) presents an image of the Pi sensor as tested in the LFACT. The Pi

sensor was constructed to exhibit a flat face with a two-inch blockage (normal to the flow direction and normal to the spanwise direction).

The second sensor was called the Omega sensor. The design geometry of the Omega sensor is depicted in Figure 8(b). An image of the Omega sensor as tested in the LFACT is presented in Figure 9(b). The Omega sensor was constructed to exhibit a circular leading edge with a two-inch diameter.

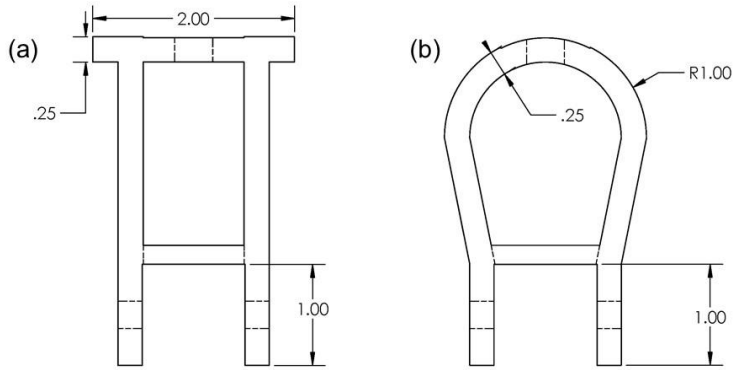

Figure 8. Top views of single waveguide geometries (inches).
Flow in LFACT is from top to bottom of figure: (a) Pi sensor and (b) Omega sensor

The collection efficiency of cylindrical leading edge exposed to clouds with typical cloud properties has been explored and well described using Langmuir-Blodgett theory (Langmuir & Blodget, 1946). The Pi sensor, which exhibited a flat surface facing the flow, was expected to have a much higher collection efficiency than the Omega sensor. However, following initial testing and initial computational fluid dynamics (CFD) and collection efficiency simulations for the Pi sensor, the collection efficiencies for the Pi sensor were not significantly different than observed for the Omega sensor. Still, the two geometries for the single sensor models allowed many operational characteristics of the sensors to be explored.

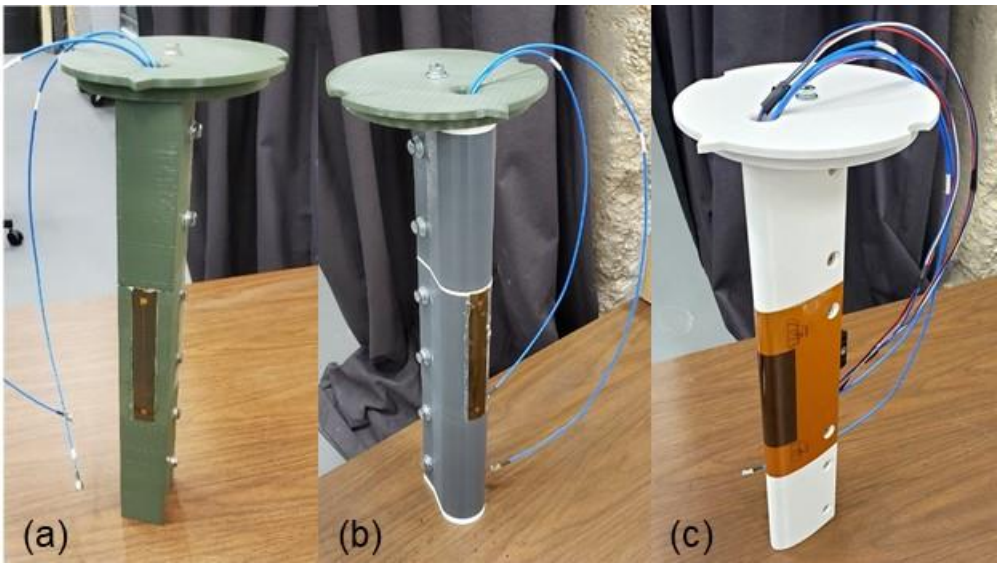

Figure 9. Models used: (a) Pi sensor, (b) Omega sensor, and (c) Multi-waveguide sensor

Each sensor body was 6-in long and constructed using a fused-deposition printer using acrylonitrile butadiene styrene (ABS) plastic. The flexible circuit boards were then epoxied to the leading edges of the sensor models. The transmission lines or waveguides on the flexible circuit boards were 0.6 mm wide and 5-in long in the spanwise direction. Two additional sections of each sensor model were printed to cover the 18-in span of the LFACT. Each sensor model was attached to a 1-in extruded aluminum support member. An end-cap with an angle-of-attack (AOA) indicator was attached to the structural member. The end-cap was attached to the LFACT test section ceiling and contained a hole for the sensor wires to pass from the sensor model to the VNA outside the test section.

4 Multi-waveguide sensor and multiplexing system

Following construction and initial testing of the single-sensor models, a multi-waveguide sensor system was created. The multi-waveguide sensor system was created for an airfoil-like surface with the intention of measuring the collection efficiency variation in the airfoil surface streamwise coordinate direction. The details of the airfoil model, multi-waveguide flexible circuit board, and multiplexing system are presented in the following sections.

4.1 Airfoil model

The airfoil model chosen for the study was a NACA 0012 airfoil. This airfoil, or two-dimensional wing shape, has been used extensively in the IRT at NASA Glenn Research Center. The symmetric NACA 0012 airfoil is a configuration commonly employed for icing investigations because the aerodynamic performance has been investigated many times and is

well understood. Additionally, the NACA 0012 is also a geometry that is publicly accessible information.

The model created for this study was selected to match the 21-in NACA 0012 that was used in multiple IRT investigations and LEWICE validation efforts. Because of the size of the airfoil relative to the size of the LFACT test section, only the first 3-in of the geometry, or the 3-in leading-edge region, was used for this effort. Figure 10(a) shows the leading-edge profile used for the multi-wire model.

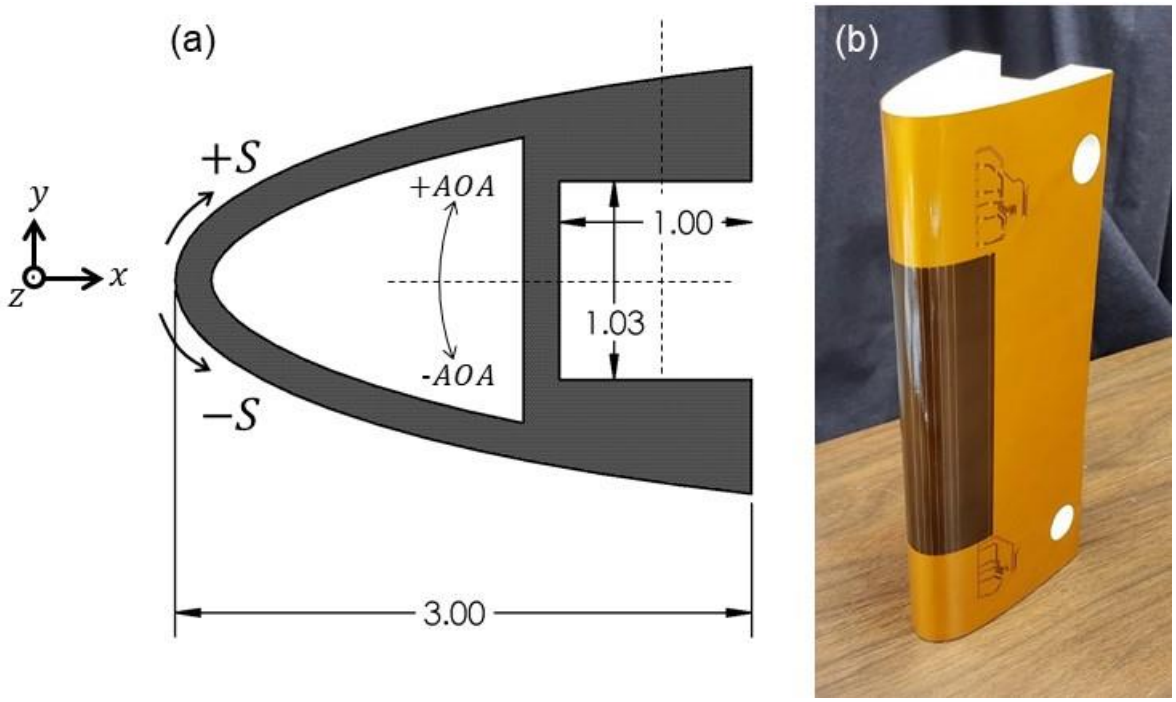

Figure 10. Multi-wire model (a) Top view and (b) Sensor body image
[Dimensions shown in inches]

4.2 Multi-waveguide sensing circuit

The multiple-waveguide sensor was created using a flexible PCB composed of Kapton film. The circuit board layout is presented in Figure 11, depicting the circuitry from the side that was eventually attached to the NACA 0012 model. The aperture or sensing area is the light blue rectangle where the waveguides are directly exposed to air. The individual sensing wires are shown in dashed dark blue lines crossing from left to right. The design uses an exposed sensing length of 4.5 inches. Four corner holes were cut from the circuit material to allow screws to pass that are needed to attach the model to a structural member and enable alignment of the circuit board to the model. Finally, the connectors and multiplexing components of the FCB are placed

in the bottom left and right. The multiplexing integrated circuits allow for the number of waveguides to occur in powers of four. Sixteen waveguides were included as four would be insufficient and sixty-four would substantially increase the design complexity. The height of the integrated circuits is less than one millimeter, but the NACA model includes rectangular cutouts so that the PCB remains completely flush.

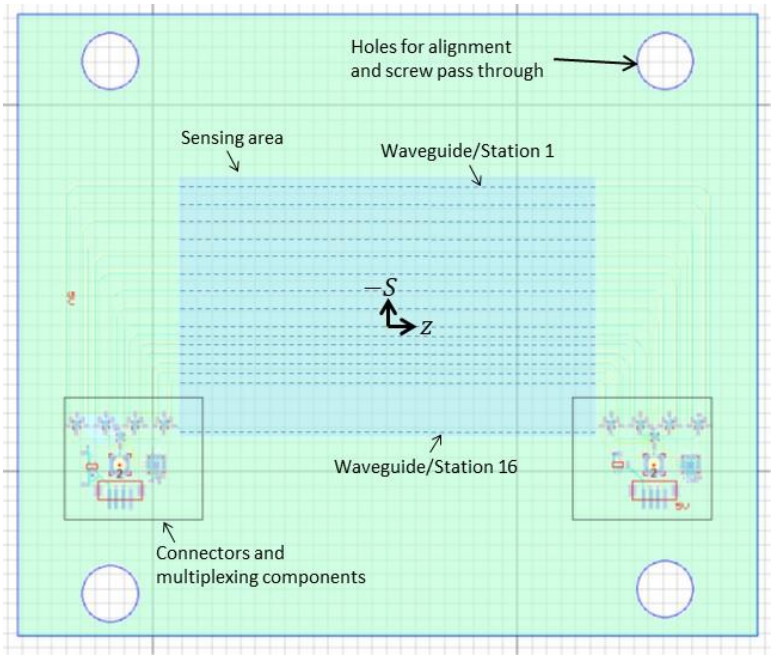

Figure 11. Multi-wire flexible circuit board diagram

The waveguide locations were placed on the flexible circuit board to enable measurements of water collection at specific locations along the surface when wrapped around the model.

Table 1 presents the waveguide locations in the surface distance along the airfoil model. The resulting X-Y projected locations in wind tunnel coordinates are also shown in Table 1. As shown in Figure 11 and as demonstrated in Table 1, a different spacing of the waveguides was used on the different sides of the model leading edge. When an airfoil or model is at an angle of attack and exposed to a cloud, the collection efficiency variation will be asymmetric about the leading edge, and the variations in collection efficiency on the suction surface of the airfoil will change abruptly. The different spacing of the waveguides was selected to provide higher resolution measurements on the suction side of the model when the model is used for investigations of the influence of AOA on surface-collection efficiency variations.

Finally, the overall length of the waveguides, which is an important operational characteristic of each waveguide, is presented in Table 1. The waveguides have the same length exposed to the

airfoil, but the different internal lengths allow for self-calibration of the PCB's effective dielectric constant.

Table 1. Waveguide locations and lengths on multi-waveguide sensor

Waveguide	S (in)	X (in)	Y (in)	L (in)
1	-1.5000	1.1845	-0.7854	13.0228
2	-1.3125	1.0046	-0.7325	12.4134
3	-1.1250	0.8268	-0.6731	11.7587
4	-0.9375	0.6518	-0.6056	11.4476
5	-0.7500	0.4814	-0.5277	10.2354
6	-0.5625	0.3161	-0.4341	9.6240
7	-0.3750	0.1689	-0.3224	8.9594
8	-0.1875	0.0499	-0.1785	8.6795
9	0.0000	0.0000	0.0000	8.1287
10	0.1000	0.0149	0.0985	7.6472
11	0.2000	0.0562	0.1893	7.1799
12	0.3000	0.1161	0.2692	7.0512
13	0.4000	0.1876	0.3390	7.3614
14	0.5000	0.2664	0.4005	6.8827
15	0.6000	0.3500	0.4553	6.4173
16	1.1250	0.8268	0.6731	5.6059

4.3 Wind tunnel model construction

The multi-waveguide sensor model body was created using ABS plastic and a fused deposition three-dimensional printer. The solid model created for the sensor body is shown in Figure 12. The important features of the multi-waveguide model were 1) countersink holes for connection to an extruded aluminum structural member, 2) four sections cut from the surface for the electrical connections to the flexible PCB, and 3) a hollow leading edge to pass the wires out of the model to the VNA.

Following printing, the flexible PCB was glued to the surface using a two-part epoxy. To keep the PCB flush with the surface, the model was mounted in a laser-cut, spanwise form that was created as a negative of the airfoil shape, and pressure was applied to the model while the epoxy cured. The model with the flexible circuit board is shown in Figure 10(b).

The cables to the waveguides and the multiplexing system were attached, and the openings to the model were filled with two-part epoxy to keep water from seeping into the circuitry. Two additional 5-in sections of the same profile as the sensor body were created using the fused-deposition printer to cover the 18-in span of the LFACT. Each sensor model was attached to a 1-in extruded aluminum support member. An end-cap with an angle-of-attack indicator was attached to the structural member. The resulting wind-tunnel model using the multi-waveguide sensor is shown in Figure 9(c).

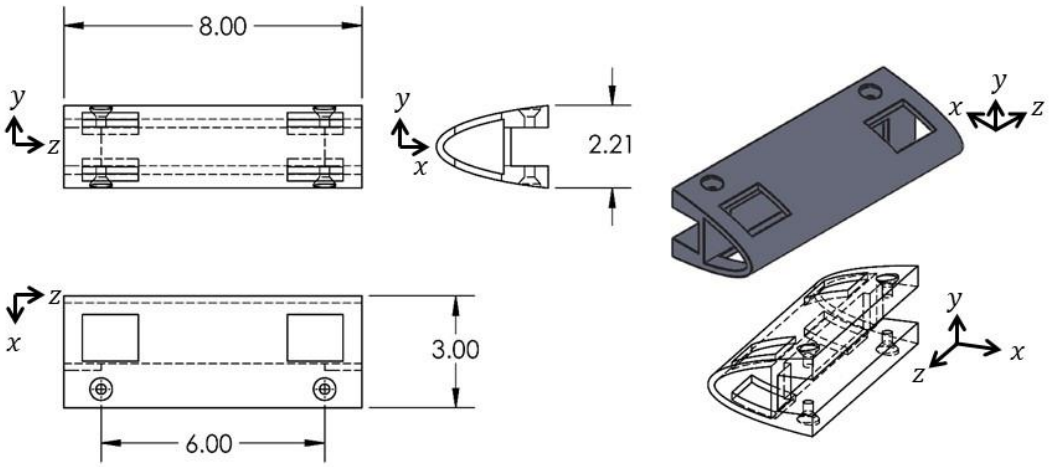

Figure 12. Line drawings of multi-waveguide sensor body [All dimensions are in inches]

4.4 Multi-waveguide sensor calibration

A second identical FCB was created and used for a calibration system. The FCB was epoxied to an acrylic plate and mounted on feet, as shown in Figure 13. The acrylic base was created with holes so that a cover with aperture could be mounted on top of the multi-waveguide sensor.

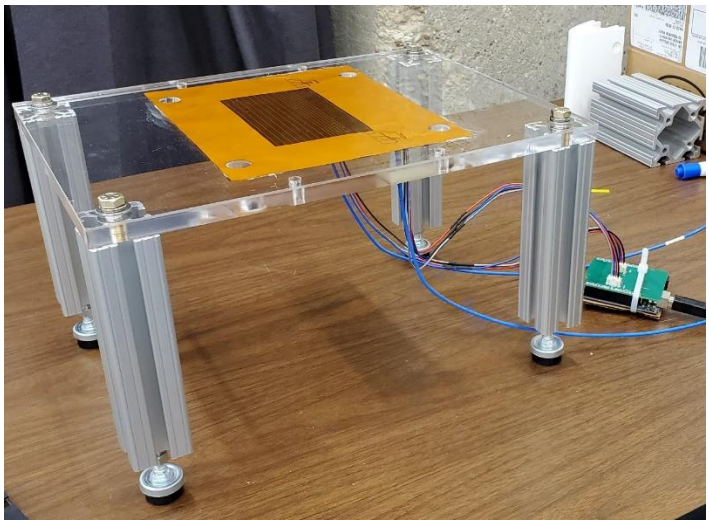

Figure 13. Multi-waveguide sensor calibration stand

A neoprene backing was applied to the cover to make the cover water-tight. The cover was attached to the calibration plate as shown in Figure 14. The aperture cut into the cover allowed specific amounts of water to be applied to the sensing area using a syringe.

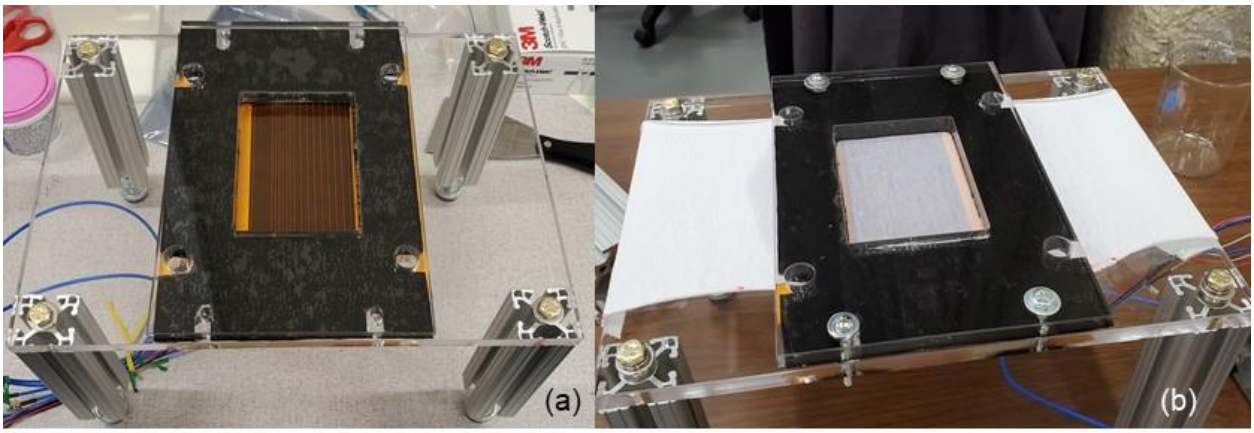

Figure 14. Multi-waveguide sensor calibration stand with aperture/window: (a) Without blotter cloth and (b) With cotton blotter strip

To determine the relative effective permittivity of the flexible circuit board (ε_{rPCB}), the propagation delay for each waveguide was measured while dry (t_{pdDRY}). Then using the known lengths ($\ell_{circuit}$) of each waveguide and the speed of light (c), the permittivity can be calculated using Equation 6.

$$\varepsilon_{rPCB} = \left(\frac{dt_{pdDRY}}{d\ell_{circuit}} * c\right)^2 \tag{6}$$

The permittivity is needed to correct for manufacturing differences of each circuit board and any changes of the PCB's substrate due to water absorption. Figure 15 shows an example of the propagation delay measurements for the multi-waveguide sensor dry calibration. The derivative method of Equation 6 allows for the calculation without needing to calibrate the feed cables.

When the sensor is in operation, the increase in relative effective permittivity due to the presence of water (ε_{rWater}) is determined by calculating the permittivity from the increase in propagation delay (Δt_{pd}) while using the 4.5 inches of exposed waveguide as the length (ℓ_{sense}). To isolate the increase in permittivity due to water from the dry circuit permittivity, the original permittivity must be subtracted with compensation for nonlinearity as shown in Equation 7.

$$\varepsilon_{rWater} = \left(\frac{\Delta t_{pd}}{\ell_{sense}} * c + \sqrt{\varepsilon_{rPCB}}\right)^2 - \varepsilon_{rPCB} \tag{7}$$

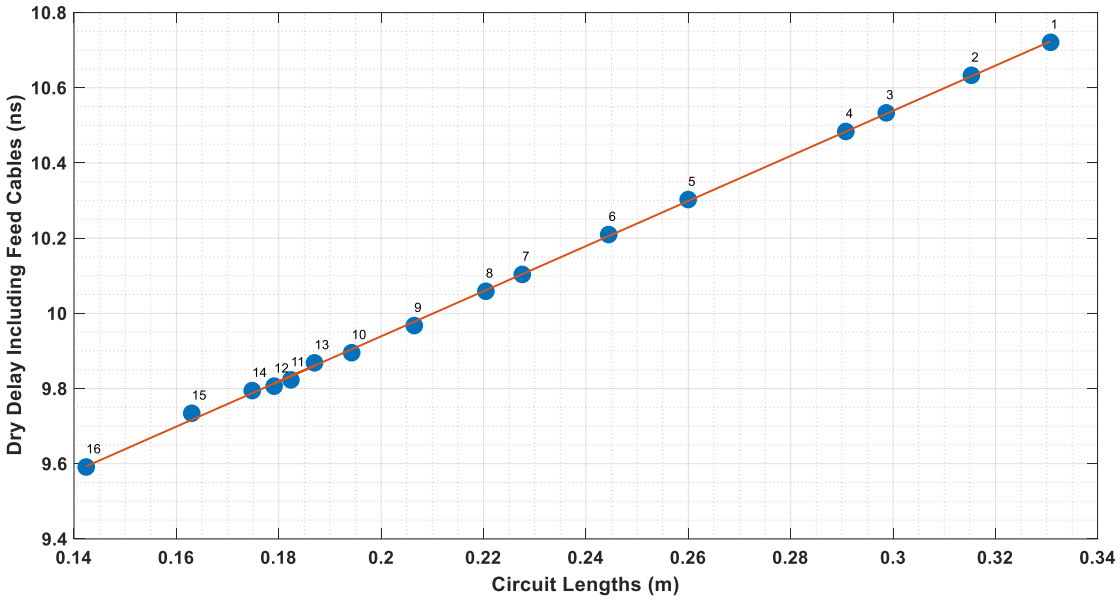

Figure 15. Relative propagation of each waveguide versus waveguide length

During the multi-waveguide sensor calibration, water was added in 1 mL increments to the calibration aperture. The water was spread to cover some of each waveguide, and the change in phase delay and the resulting increase in permittivity was calculated for each waveguide. The change in phase delay or permittivity was then averaged across all sixteen waveguides.

Figure 16 presents the calibration results in terms of the average increase in permittivity as water was added to the aperture. The calibration was performed in Direct mode, where water was directly applied to the sensor face, and in Blotter mode, where a piece of cotton cloth was stretched over the sensor as shown in Figure 14(b). Dry sensor permittivity calculations are done once for each method as the blotter cloth changes the effective permittivity slightly. Just as water

molecules are polar, the cellulose molecules of cotton are polar. However, the low density of the cotton results in cloth permittivity's between 1 and 2, but the cloth must be compensated for so t_{pdDRY} effectively becomes $t_{pdDRYCLOTH}$.

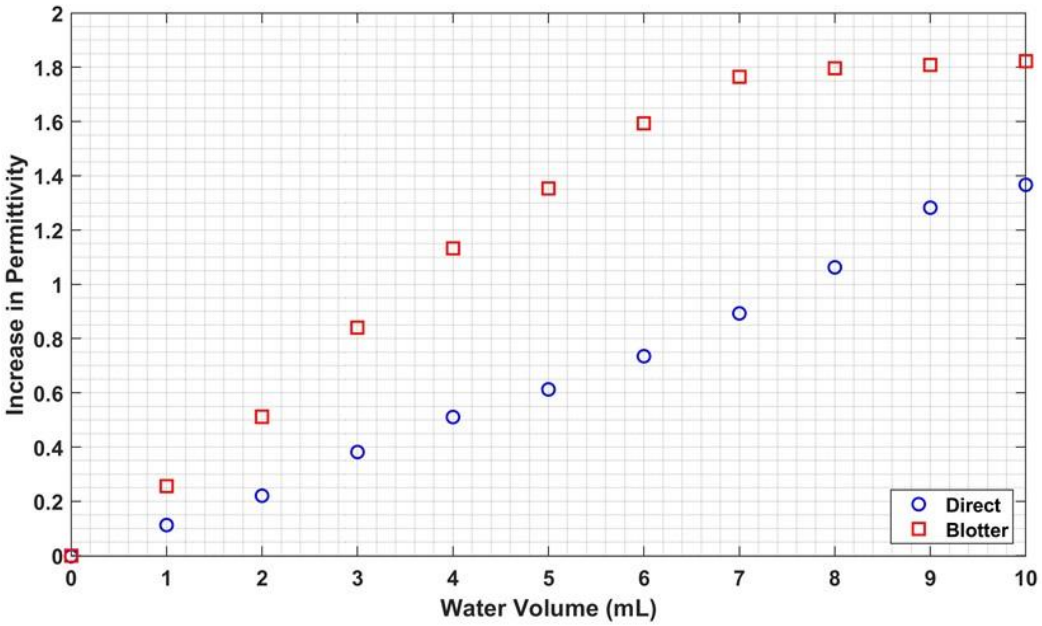

Figure 16. Calibration results with blotter cloth and with direct measurement

The increase in permittivity was expected to be linear with respect to the amount of water added to the aperture based on an even spreading of the water among the sensor waveguides. The difference in two calibration results of Figure 16 relate to the pooling of the water on the surface of the aperture. When calibrating Direct measurements, the water in the sensor area pooled or formed connected beads that were taller than the sensing distance of the waveguides from the initial addition of water to the aperture area. Additionally, leakage from the calibration stand gaskets was noticed when in Direct mode.

When calibrating with the blotter cloth, the water was wicked around the waveguides more evenly. Since permittivity is a volumetric measurement having more uniform water distribution in the blotter cloth increased the sensitivity. At volumes above 7mL complete coverage and saturation of the aperture area with water was noticed.

5 Wind tunnel modifications

All testing was performed in the LFACT at Baylor University. The LFACT is a low-speed wind tunnel with an 18-in by 18-in test section. The inlet settling chamber and 6.25:1 contraction were constructed by ELD, Inc. A Hartzell marine-rated fan can generate speeds over 30 m/s, but with

the 2-in flat single-sensor model in the tunnel, the maximum velocity achievable is 22 m/s. A side view schematic of the LFACT is shown in Figure 17, and an image of the LFACT is presented in Figure 18.

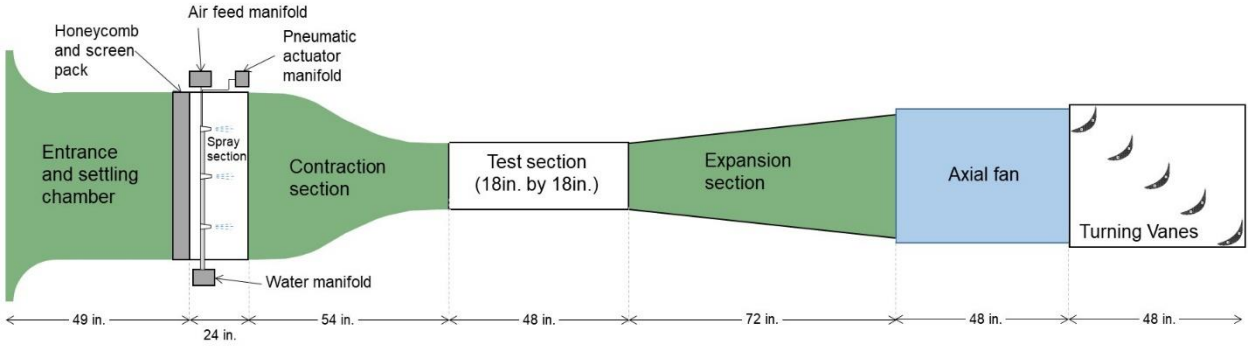

Figure 17. Side view (not to scale) of liquid film and cloud tunnel (LFACT)

Figure 18. Image of LFACT and supporting equipment

The spray section and the turning vane section were constructed during this study. The details of the spray section, the spray control system, and the turning vane section are discussed in the next sections.

5.1 Spray nozzle section

The spray section of the LFACT was replaced for the current study. The original spray section was based on liquid pressure nozzles only with passive droplet size control and was intended for steady state humidity and cloud property measurements. Additionally, the original spray system did not have electronic control or fast actuation, which were required for collection efficiency measurements.

The nozzle that was selected to accomplish this is the 1/8JJAU nozzles with SU11 setups that is produced by Spraying Systems Co. The 1/8JJAU can have a variety of different spray setups that are determined by the air cap and fluid cap attached to the nozzle. Since the flow rates desired were low (0.533 gph), the SU11 spray setup was chosen. This setup is a pressure spray setup for internal mix and round spray.

An example 1/8JJAU nozzle with the SU11 setup is shown in Figure 19. Since the nozzles are pneumatically controlled, air assisted nozzles, each nozzle requires three inlet lines: 1) an air feed line, 2) a water feed line, and 3) a pneumatic control feed line. Each line is depicted in Figure 19(a). A fourth line is also shown in Figure 19(a), which is an air-feed pass through so that multiple nozzles may be fed in series from one air manifold.

The spray bar system consists of nine of these 1/8JJAU nozzles on a three-by-three square pattern. The flow area of the spray section is 45-in by 45-in. The outside nozzles were placed 7.5 in from the walls, and the spacing between each nozzle was 15 in. The resulting spray section is shown in Figure 20.

The supply manifolds for the nozzles are also visible in Figure 20. Each manifold was created using extruded aluminum structural members. The water manifold was mounted below the spray section, and the air feed manifold and the pneumatic control manifold were mounted on top of the spray section. The tubing used to deliver air and water from each manifold to the nozzles are discernable in Figure 20 as well as in Figure 19(a) and Figure 19(b). Finally, the nozzles were mounted on three aluminum struts, which are also visible in Figure 20, Figure 19(a), and Figure 19(b).

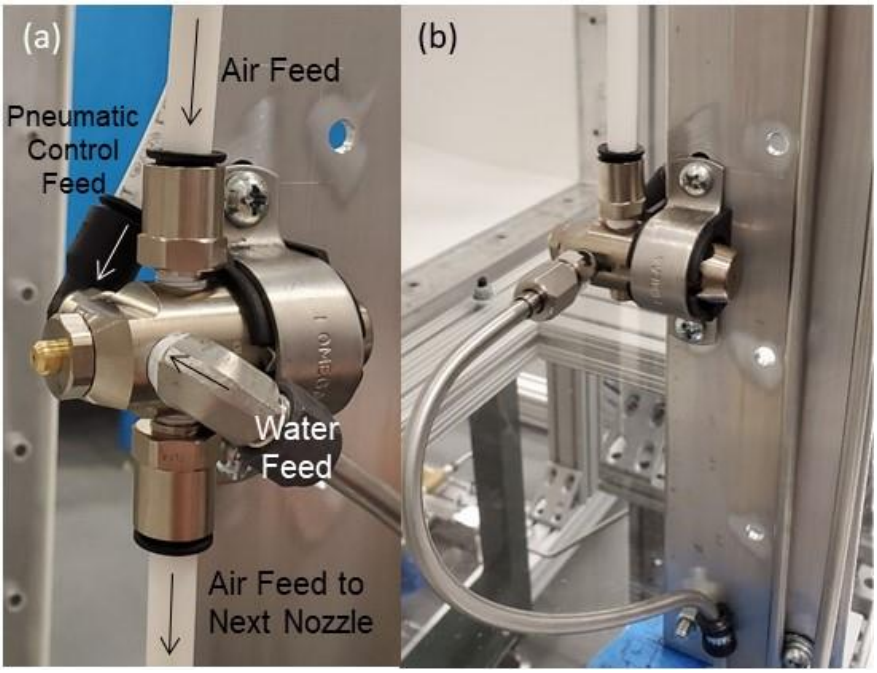

Figure 19. Air-boost spray nozzle installation: (a) Front-side view, (b) Rear-side view

Figure 20. Spray nozzle section of LFACT

5.2 Spray control panel

A spray or pressure control panel was created to contain the pressure regulators, pressure tank, flowmeter, and the corresponding electronics. The pressure regulators control the amount of pressure to the air feed line, the pneumatic control line, and the water feed line with the use of a pressure-transducer feedback system. For each line, air is supplied by the building compressed air system. The water system setup is like the air feed lines, but the pressure regulator controls pressure in the air above the deionized water in a tank that is supplied to the nozzles. The pressure control panel is shown in Figure 21(a).

The pressure regulator assembly is a pilot operated diaphragm style regulator and includes a flow booster. The regulator is controlled using a data acquisition system and a voltage analog output card. The regulator reads the desired voltage from the output card, then increases flow until the voltage from the pressure transducer matches the voltage from the analog output card. One of the three electronic regulators is shown in Figure 21(b).

A turbine flow meter, shown in Figure 21(c), was also installed on the pressure control panel. The flowmeter was installed between the deionized water tank and the water feed manifold. The turbine flowmeter was used to verify flow characteristics reported by the nozzle manufacturer as well as to verify nozzle actuation and timing. However, the presence of the flowmeter between the tank and the water manifold caused a considerable drop in pressure between the tank, where the regulator was attempting to operate, and the water manifold, where the feedback pressure transducer was installed. While the issues were not a problem in steady-state spray operation, when fast actuation and stopping of the cloud were required, the flowmeter was bypassed using a ball valve system shown in Figure 21(c).

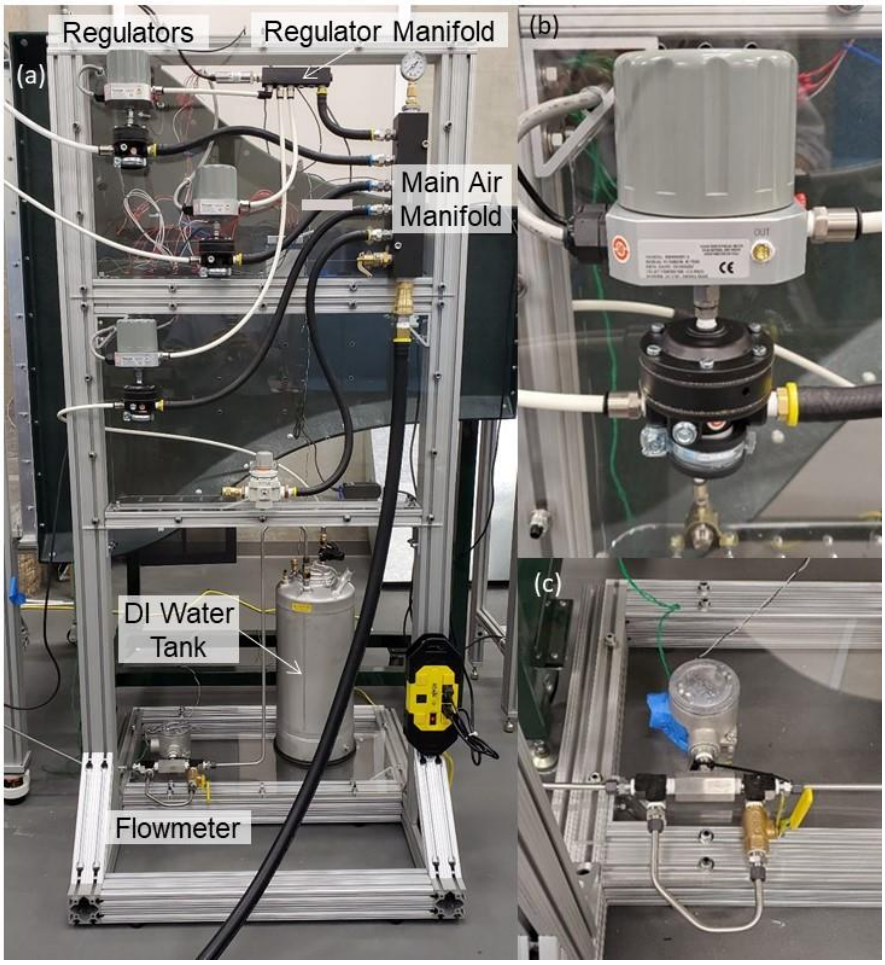

Figure 21. Spray bar control system:
(a) System diagram, (b) Electronic regulator, and (c) Turbine flowmeter

5.3 Turning vanes and droplet capture

A set of turning vanes at the exit of the wind tunnel was required for this study. The turning vanes were created using extruded aluminum structural members, sheets of Lexan, and vanes that were constructed using ABS plastic over aluminum rods. The turning vanes, shown in Figure 22, were designed with solidity of 1.05. This solidity was used so the turning vanes functioned as a droplet capture system. The droplet capture system was required to keep elevated levels of water from flowing into the space behind the doors of the lab which can also be seen in Figure 22.

Figure 22. Flow turning vanes and droplet capture system:
(a) System as installed and (b) System in operation during a cloud LWC uniformity test

6 Single waveguide sensor and multi-waveguide sensor behavior

The two single waveguide sensors and the multi-waveguide sensor were tested in the LFACT for different purposes. Figure 23 shows the Pi Sensor and the multi-waveguide installed in the LFACT. The following subsections detail the measurements with each sensor and the observations regarding collection efficiency measurements.

Using the single-waveguide sensors, aspects of sensors operation were identified and explored. Because the single-waveguide sensors were less complex than the multi-waveguide sensor, the single-waveguide sensors were used to test data acquisition components of the wind tunnel, the spray bar system, the VNA, and the microwave circuits. The timing of the VNA measurements relative to the triggering or actuation of the spray-bar system was also finalized using the single-waveguide sensors.

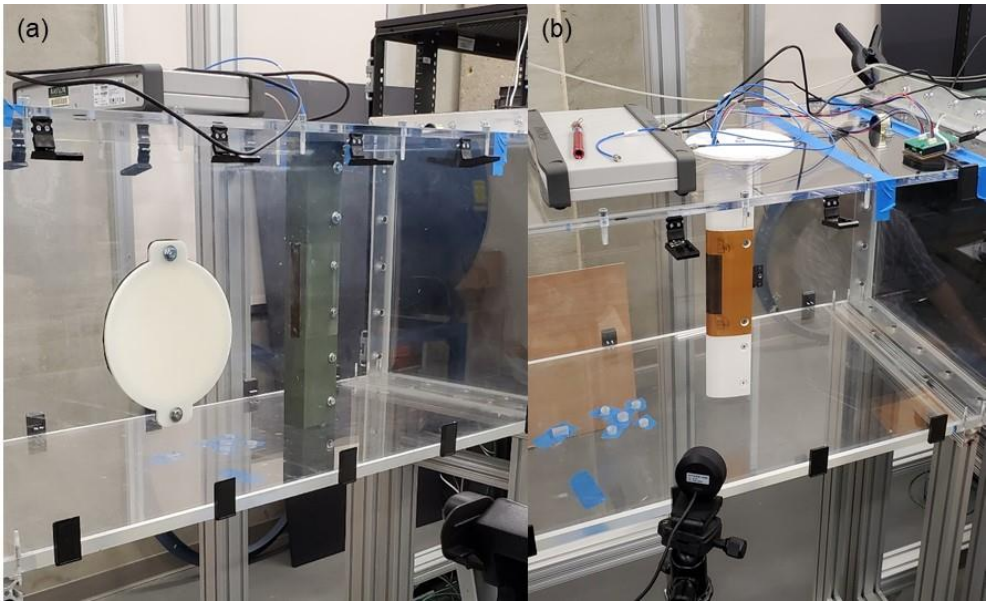

Figure 23. (a) Pi sensor and (b) Multi-waveguide sensor as installed in the LFACT

Following the identification of operating and data collection approaches, the two primary investigations with the single-waveguide sensors were 1) demonstration of single sensor repeatability under exposure to clouds with different droplet sizes and 2) investigation of sensor response to changes in the model AOA. The different droplet sizes for the repeatability case were chosen as a middle-range Appendix C case (~30 μm) and a near SLD case (~50 μm) (Aeronautics and space, airworthiness standards: transport category airplanes) and (Airplane and engine certification requirements in supercooled large drop, mixed phase, and ice crystal icing conditions, 2015). The AOA study was performed because the variation of collection efficiency for the Omega Sensor was expected to follow the variation along the surface of a cylinder in cross-flow. Additionally, the collection efficiency of the Pi Sensor was expected to be higher and less sensitive than for the Omega Sensor.

The operating conditions for the single-waveguide sensor tests are presented in Table 2. The information in Table 2 for the Median Volumetric Diameter (MVD) values and the flow rates per nozzle are based on the nozzle manufacturer specifications. The liquid water contents provided in Table 2 are then based on the assumption of an evenly distributed cloud through the test section and calculated using Equation 8.

$$LWC_D = \frac{9Q_{Noz}\rho_w}{V_\infty A_t} \tag{8}$$

Table 2. Operating pressures and conditions based on nozzle information from manufacturer for the single-waveguide sensor tests

Case Set	V_∞ *(m/s)*	P_{air} *(psi)*	P_{H2O} *(psi)*	MVD *(μm)*	Q_{Noz} (gph)	LWC_D (gm/m^3)	Δt_s (s)
Repeat1	22	20	18	27	0.78	1.61	5
Repeat2	22	10	7.4	47	0.34	0.69	10
AOA1	22	10	7.4	47	0.34	0.69	10
AOA2	22	20	14.4	18	0.35	0.73	10

6.1 Pi sensor performance

The performance of the Pi sensor is described in the following two subsections. As described earlier, the Pi sensor was constructed with a flat surface perpendicular to the flow to have a collection efficiency near 1.0.

6.1.1 Repeatability

The repeatability investigation was performed by triggering the spray system to produce a cloud for a predetermined exposure time. At the same time the cloud was triggered, the VNA was triggered to start sampling from the waveguide over the duration of the spray plus an additional amount of time to see the sensor begin drying out. Since the single-waveguide sensors were not calibrated for direct mass measurements, the repeatability measurements were reported in terms of the propagation delay, as defined in Equation 5.

Figure 24 presents the results of five repeated tests for the two cases identified in Table 2 as Repeat cases. The results for the 27-μm case are reported in Figure 24(a), and the results for the 47-μm are shown in Figure 24(b).

For both sets of cloud conditions, the sensors responded as expected. At the beginning of each spray, the propagation delay increased linearly and then approached an unsteady asymptotic state. The asymptotic nature was caused by the formation of a quasi-steady film thickness at the location of the waveguide, and the unsteadiness was caused by the formation and shedding of beads that ran along the surface because of flow pressure and shear.

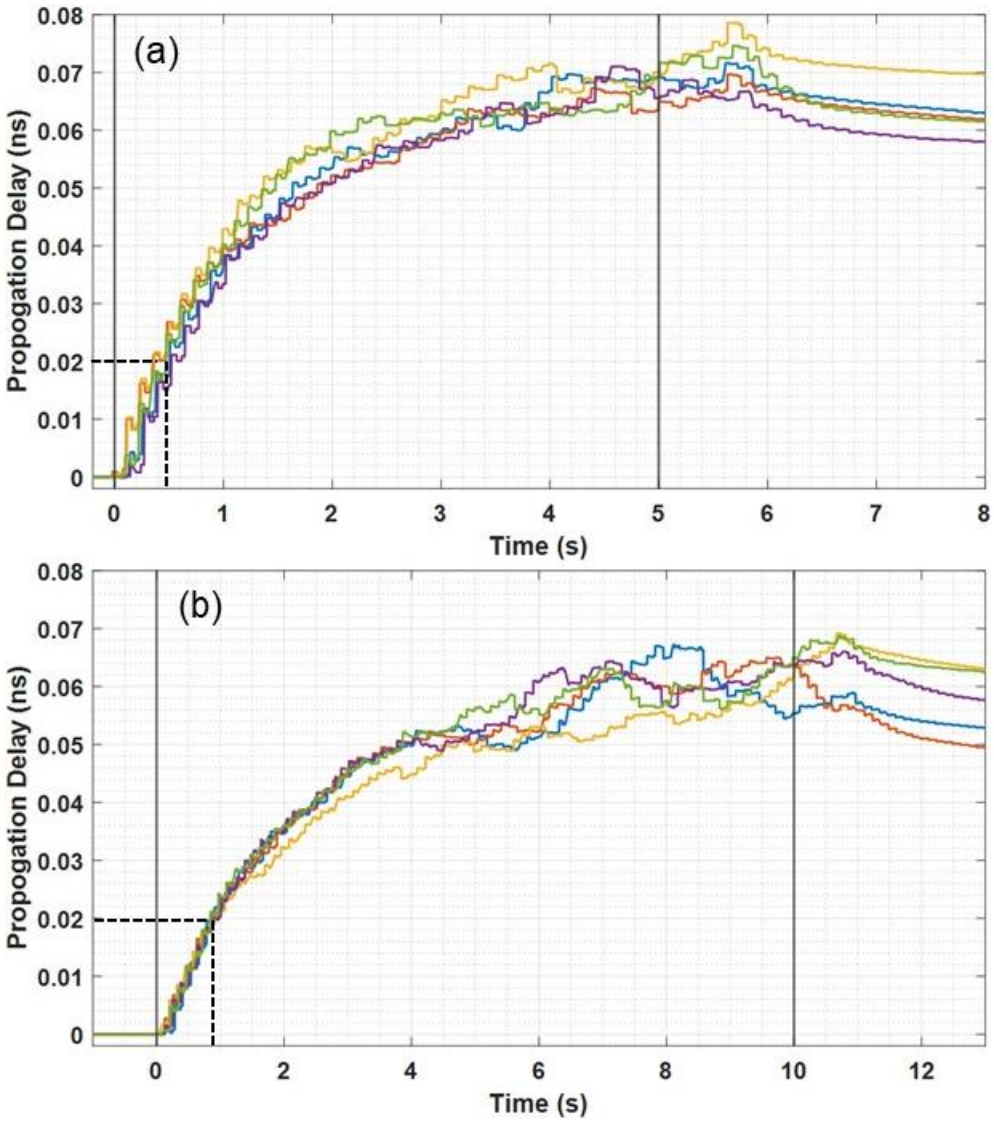

Figure 24. Repeatability results from the Pi sensor
(a) P_{air} = 20 psi, P_{H2O} = 18 psi, MVD = 27 μm, and (b) P_{air} = 10 psi, P_{H2O} = 7.4 psi, MVD = 47 μm

Figure 24(b) demonstrates that the five curves collapse more tightly for the 47 μm cases than observed for the 27 μm of Figure 24(a).

Revisiting Table 2, the manufacturer specified nozzle volumetric flow rate for the 27 μm case was more than twice that for the 47 μm case. The variability in the 27 μm cases was caused by the fact that at the higher flow rates, the spray bar system took longer to actuate and was less precise than for the lower flow rate. However, the dashed lines indicate that the time required for the 47 μm cases to reach a propagation delay of 0.02 ns was approximately twice the time required for the 27 μm cases. Because of the actuation accuracy and the longer times for the

linear sensor response, the AOA investigation used two cases that were both at the lower volumetric flow rate of ~0.34 gallons per hour per nozzle.

6.1.2 Angle of attack variations

Following the repeatability tests, an AOA sensitivity study was performed. For this study, the Pi Sensor was rotated around the spanwise axis in increments of 5° from 0° to 20°. For each AOA, a 10 second spray was triggered while the VNA sampled for 13 seconds at each AOA for two cloud conditions reported in Table 2. As with the repeatability cases, the single-waveguide sensors were not calibrated for direct mass measurements. The AOA measurements were reported in terms of the propagation delay, as defined in Equation 5, and the resulting propagation delay measurements of the AOA study are shown in Figure 25.

Figure 25 demonstrates that the Pi Sensor was sensitive to the changing AOA, and that the changes followed the expected trends of decreasing measured propagation delay at a specific moment during the test with increasing AOA. That is, focusing on the zero-one second regions of each test, the propagation delay at one second, decreased as the AOA was increased from 0° to 20°. While the results do follow the expected trend, some of the trend lines overlap for the different AOAs. The overlapping of 5° to 15° trend lines was caused by the minor changes in collection rates, the spatial variations in the cloud properties, and the repeatability in cloud timing between the tests.

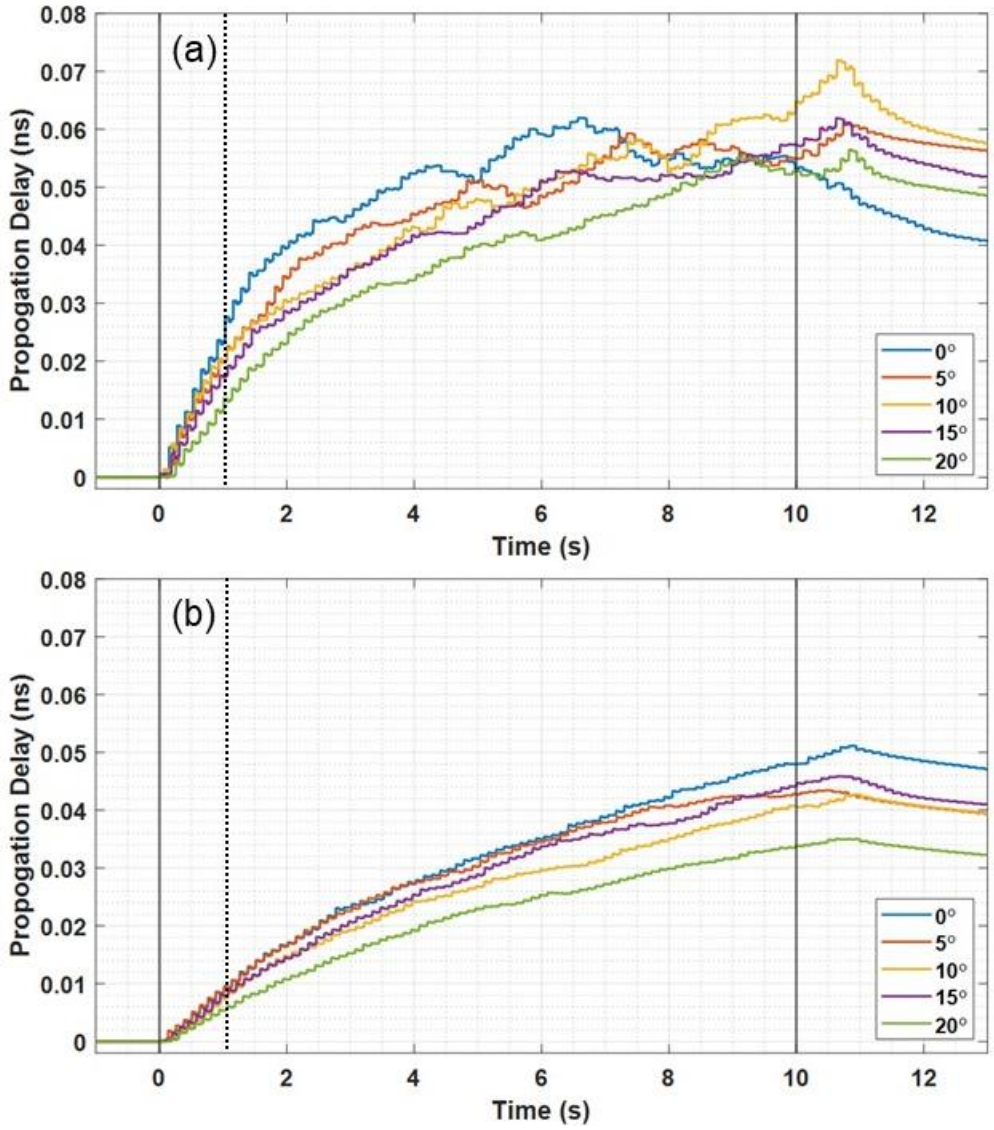

Figure 25. Pi sensor angle of attack variation results
(a) P_{air} = 10 psi, P_{H2O} = 7.4 psi, MVD = 47 μm, and (b) P_{air} = 20 psi, P_{H2O} = 14.4 psi, MVD = 18 μm

6.2 Omega sensor performance

The performance of the Omega sensor is described in the following two subsections. As described earlier, the Omega sensor was constructed to have a cylindrical leading edge with a radius of 2.54 cm (1.0 in). The circular leading edge was chosen because it is the basis of Langmuir-Blodgett theory for leading-edge collection efficiency.

6.2.1 Repeatability

Just as was performed for the Pi sensor, the repeatability investigation was performed by triggering the spray system to produce a cloud for a predetermined exposure time. At the same

time the cloud was triggered, the VNA was triggered to start sampling from the waveguide over the duration of the spray plus an additional amount of time to see the sensor begin drying out.

Figure 26 presents the results of five repeated tests for the two cases identified in Table 2 as Repeat cases. The results for the 27-μm case are reported in Figure 26(a), and the results for the 47-μm are shown in Figure 26(b).

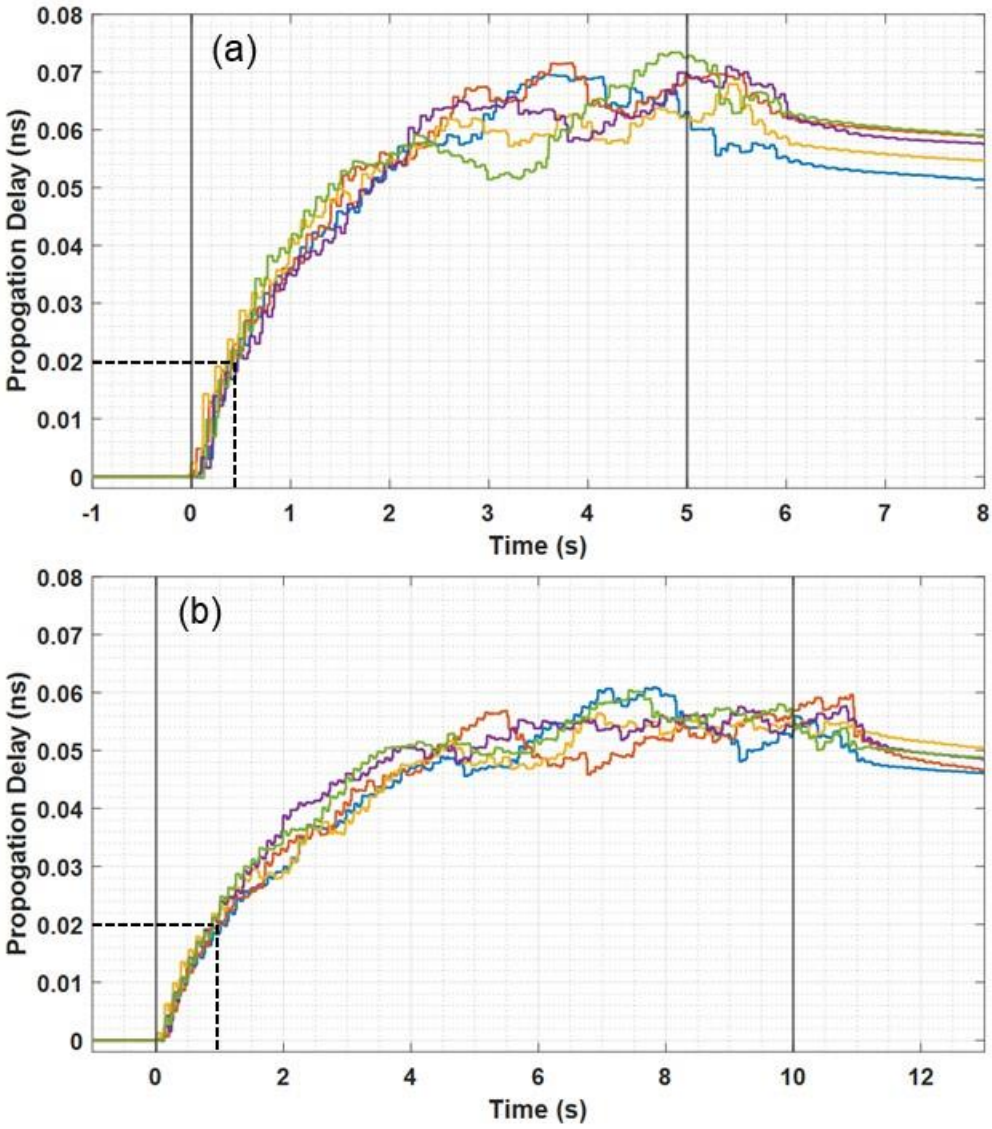

Figure 26. Repeatability results from the Omega sensor
(a) P_{air} = 20 psi, P_{H2O} = 18 psi, MVD = 27 μm, and (b) P_{air} = 10 psi, P_{H2O} = 7.4 psi, MVD = 47 μm

Figure 26(a) and 26(b) demonstrate that the five curves collapse for both the 47-μm cases and the 27-μm cases. The agreement for each case for the Omega sensor cases was qualitatively better than for the Pi sensor. The dashed lines in Figure 26 indicate the one second required for

the cases to reach a propagation delay of 0.02 ns, which is shown to be the amount of water collection observed with repeatability due to no bead run-back. For each condition, the time required was more tightly packed than for the Pi sensor.

6.2.2 Angle of attack variations

An AOA sensitivity study was also performed for the Omega sensor. As was performed for the Pi sensor, the Omega sensor was rotated around the spanwise axis in increments of 5° from 0° to 20°. For each AOA, a 10 second spray was triggered while the VNA sampled for 13 seconds at each AOA for two cloud conditions reported in Table 2. Again, the single-waveguide sensors were not calibrated for direct mass measurements, so the AOA measurements were reported in terms of the propagation delay, as defined in Equation 5. The resulting propagation delay measurements of the AOA study for the Omega sensor are presented in Figure 27.

The results of Figure 27 demonstrate that the Omega sensor was sensitive to the changing AOA, and that the changes followed the expected trends of decreasing measured propagation delay at a specific moment during the test with increasing AOA. That is, focusing on the zero-one second regions of each test, the propagation delay at one second, decreased as the AOA was increased from 0° to 20°. As was the case with the Pi Sensor, some of the trend lines overlap for the different AOAs. The overlapping of 5° to 15° trend lines was caused by the minor changes in collection rates, the spatial variations in the cloud properties, and the repeatability in cloud timing between the tests (Fujiwara & Bragg, 2019).

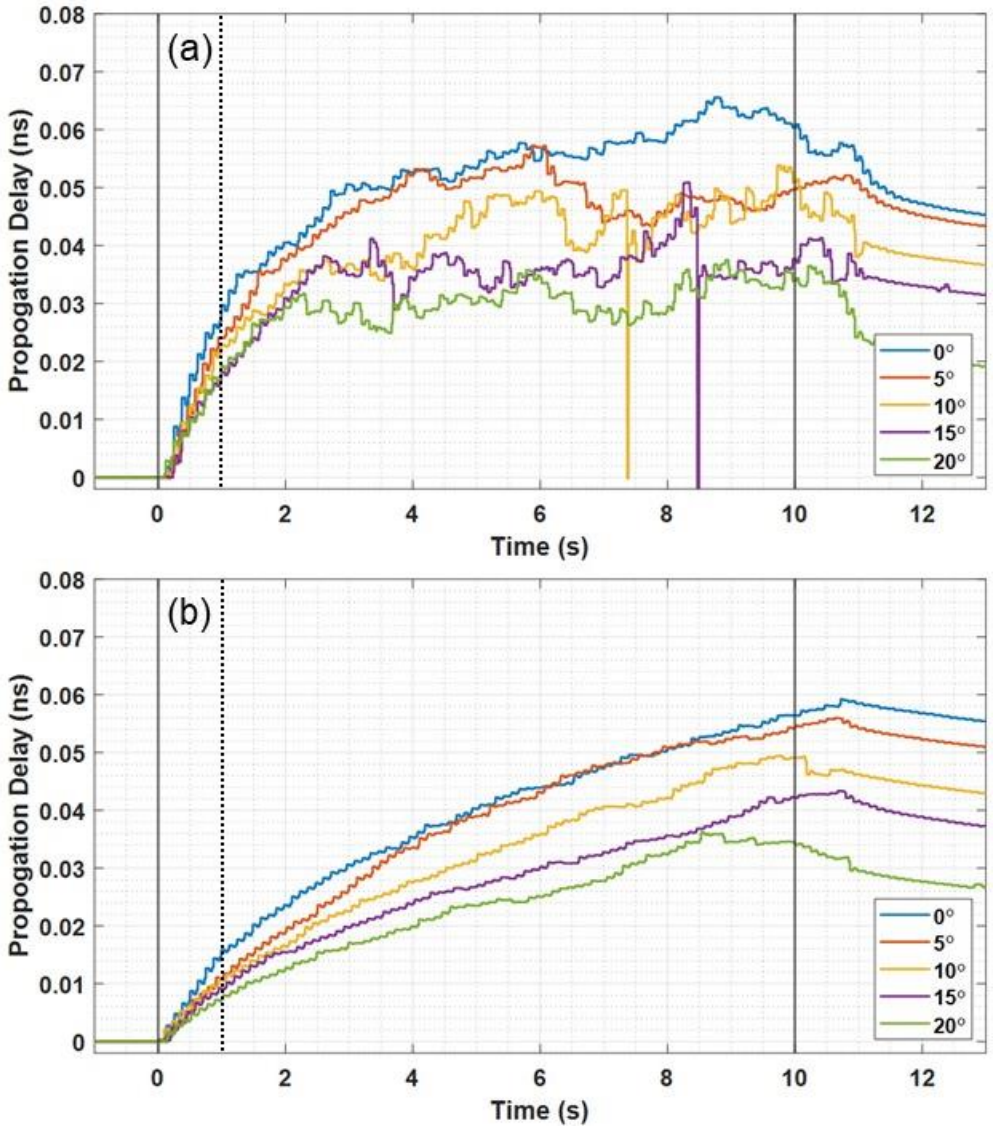

Figure 27. Omega sensor angle of attack variation results
(a) P_{air} = 10 psi, P_{H2O} = 7.4 psi, MVD = 47 μm, and (b) P_{air} = 20 psi, P_{H2O} = 14.4 psi, MVD = 18 μm

6.3 Single waveguide sensor summary

The single waveguide sensors were used to explore basic response of the sensors to transient cloud exposures in preparation for subsequent tests using the multi-waveguide sensors. The single sensor measurements demonstrated 1) the physics and operating principle of the sensors were viable, 2) the sensors were responsive and responded as expected to an abruptly initiated cloud exposure, 3) the linear sensing times of the sensors without a blotting or capture surface was on the order of one second, and 4) cloud repeatability in the LFACT was affecting the sensor repeatability tests and the AOA sensitivity tests.

6.4 Multi-waveguide sensor performance

Following the single-waveguide sensor study, the multi-waveguide model was used to explore how the microwave system might be implemented in a larger icing wind tunnel such as the IRT. Specifically, three modes of testing were explored. The first mode was Sequential Direct Transient where each individual waveguide was sampled continuously during a spray. The second mode was Steady State Film, where all the waveguides were sampled consecutively during a long spray to evaluate the steady state film thickness. The third operational mode was to wrap the multi-waveguide model with either paper or cotton, like part of the approach used by Papadakis et al. (2007) to capture and hold the water at the surface.

When one of the operational modes was determined to be useful, an approach like that performed for the single waveguide sensors was used to investigate sensor repeatability and AOA sensitivity. However, the cases used for the repeatability cases for the multi-waveguide sensor were different from the repeatability cases for the single waveguide sensors. Table 3 presents the conditions for the multi-waveguide sensor tests.

Table 3. Operating pressures and conditions based on nozzle information from manufacturer for the multi-waveguide sensor tests

Case Set	V_∞ *(m/s)*	P_{air} *(psi)*	P_{H2O} *(psi)*	*MVD* *(μm)*	Q_{Noz} (gph)	LWC_D (gm/m^3)
AOA1	22	10	7.4	47	0.34	0.69
AOA2	22	20	14.4	18	0.35	0.73
Repeat1	22	10	8.6	52	0.51	1.04
Repeat2	22	20	15.6	21	0.50	1.02

6.4.1 Sequential direct transient waveguide measurements

The first mode of operation tested was the Sequential Direct Transient measurements. In this case, a single waveguide was sampled continuously during a spray event. The model was dried, and the subsequent waveguide was tested under the same conditions. For the multi-waveguide sensor, this operational mode resulted in sixteen individual tests to fully characterize the surface variations in water collection when exposed a specific cloud condition. Additionally, this mode of operation requires that the cloud conditions generated by the LFACT for the 16 tests to be repeatable.

Figure 28 presents the responses of the sixteen waveguides in response to a three-second spray under the conditions identified as AOA2 in Table 3. In Figure 28, the response of each waveguide is characterized in terms of the increase in relative permittivity from the dry permittivity of the FCB. Figure 28 demonstrates that following the initiation of the cloud, the relative permittivity increases and then decreases following the end of the spray. The linear region over the 0-1 second is then used to characterize the rate of increase in permittivity associated with each waveguide. The rate of increase in permittivity indicates the rate of water collecting on the surface and is the y-axis of Figure 29 and reported in units of permittivity per second.

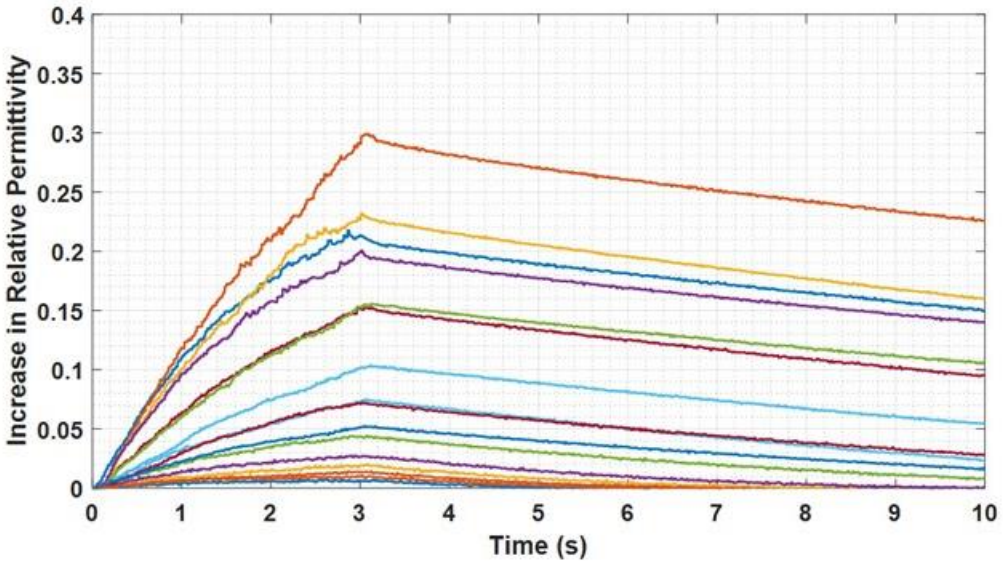

Figure 28. Transient measurements of relative permittivity for each waveguide exposed to the same cloud properties [P_{air} = 20 psi, P_{H2O} = 14.4 psi, MVD = 18 μm]

The resulting comparison of each waveguide transient response to the cloud conditions identified as AOA1 and AOA2 in Table 3 are presented in Figure 29. The resulting variations in the rate of permittivity increase along the surface distance exhibits variations in the form of asymmetry and slight increases on one side of the leading edge that were not expected based on prior reported simulations in LEWICE (Wright, 2008). The suspected cause of the variations was lack of consistency in the generation of the clouds in the LFACT.

To improve the consistency in the cloud generation, an automated system was developed using LabVIEW to sample each waveguide sequentially without operator intervention between the tests. Sufficient time was programmed into the control software such that the surface of the model dried between the tests. The results of the automated tests are compared to the manual tests in Figure 29. The automation system did not significantly improve the variation in the

permittivity increase rates. Because of the variations in the collection rates along the surface and because of the significant time required to perform sixteen waveguide tests for each model and each cloud condition, the Sequential Direct Transient was found unsuitable for implementation in larger-scale wind tunnels such as the IRT at NASA Glenn Research Center.

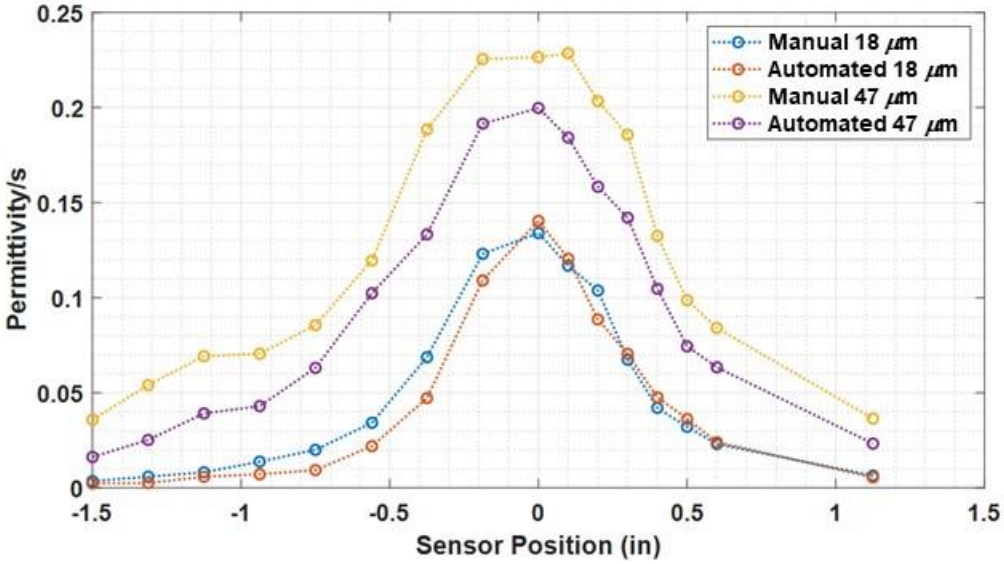

Figure 29. Rate of permittivity increase during the first second of transient spray of each waveguide versus the waveguide's surface distance location along model

6.4.2 Steady-state liquid film measurements

The second mode of operation explored using the multi-waveguide sensors was the Steady-State Film measurements. In this mode, a continuous cloud spray was used. Following approximately 30 seconds of established spray, each sensor was sampled for 30 seconds consecutively while the spray was maintained.

Figure 30 presents the increase in permittivity from the dry condition for each waveguide over the 30 seconds of sampling for the condition identified as AOA2 in Table 3. The significant variations in the increase in relative permittivity exhibited in Figure 30 is caused by the shedding or running of beads over each waveguide. The running beads are visible on the model in Figure 31, which presents a still image taken from a video from an AOA2 case.

The resulting increase in relative permittivity for each waveguide is presented in Figure 32 versus the surface location of the waveguide from the leading edge of the model. The variation shown in Figure 32 demonstrates that while the steady-state film thickness measurements generally followed the expected trends in collection efficiency, the film dynamics, and the

shedding and runback of the beads made the approach unreliable for inferred collection efficiency measurements.

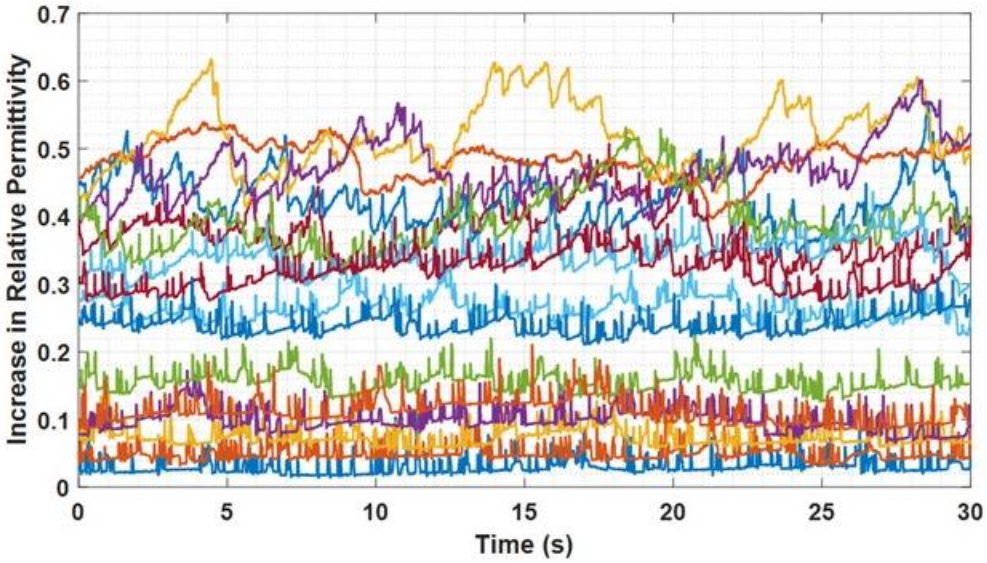

Figure 30. Steady permittivity measurements of each waveguide sampled consecutively during continuous spray [P_{air} = 20 psi, P_{H2O} = 14.4 psi, MVD = 18 μm]

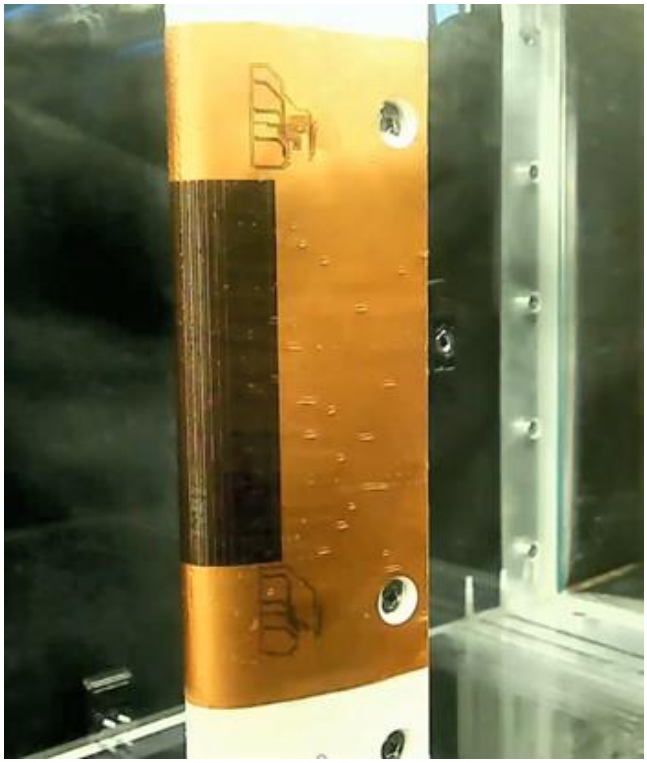

Figure 31. Image from video taken during steady film thickness measurements showing running beads on model

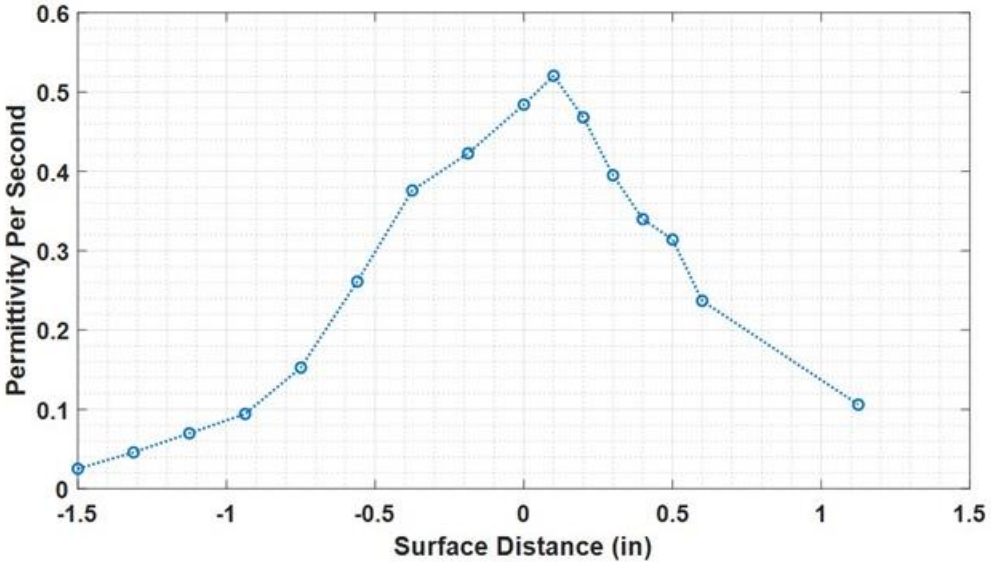

Figure 32. Average steady increase in permittivity (from dry condition) versus waveguide location on model [P_{air} = 20 psi, P_{H2O} = 14.4 psi, MVD = 18 μm]

6.4.3 Initial blotter paper and cloth measurements

The third mode of operation for the multi-waveguide sensor was like the blotter paper approach used by Papadakis et al. (2007). In the Blotter Paper/Cloth approach, an absorbing material was stretched across the surface of the model. A brief spray was actuated, then immediately following the end of the spray, the waveguides were sampled sequentially to determine the change in permittivity. The presence of the blotter paper or cloth captures the water from the cloud and holds it near the surface for measurement by the waveguides.

In initial testing using paper as the blotter or capture material, the paper stretched and separated from the model surface. The paper used was not the same weight blotting paper as used by Papadakis et al. (2007). For all subsequent tests, a cotton cloth was stretched around the model and used for all subsequent Blotter Cloth measurements.

In reviewing the requirements that were identified by Papadakis et al. (2007), the use of cotton increases the surface resistance, but at the speeds investigated, the effects should not be significant. The cotton cloth is a less dense weave than the blotter paper used by Papadakis et al., and other than the fact that the less dense weave will spread out the water among the fibers more effectively, the full importance of the weave density is not currently known. However, the use of cotton capture medium allowed the reuse of the cloth if the cloth was dried following a test.

During LFACT testing, the phase delay was measured following tests, and the next test was not initiated until the dry phase delay was measured for the leading edge waveguide.

Figure 33 presents the results of blotter cloth measurements as part of an AOA investigation using the multi-waveguide sensor. For the AOA1 and AOA2 conditions identified in Table 3, the response of all waveguides was determined following a 10 second spray at -4°, 0°, and 4° angles of attack. In Figure 33, the increase in relative permittivity at each waveguide is plotted as a function of surface position of the waveguide along the sensor.

Focusing initially on the 0°-AOA results in Figure 33, the waveguides are sensing different mass accumulations when exposed to the two different cloud conditions of AOA1 and AOA2. The variation for each cloud condition case is also responding as expected in that 1) the maximum increase in relative permittivity, which relates directly to the amount of water collected at the waveguide location, occurs at the leading edge of the model and 2) the increase in relative permittivity decreases with increasing surface distance from the leading edge. However, the variations in the increase in relative permittivity do not exactly follow the expected trends in collection efficiency.

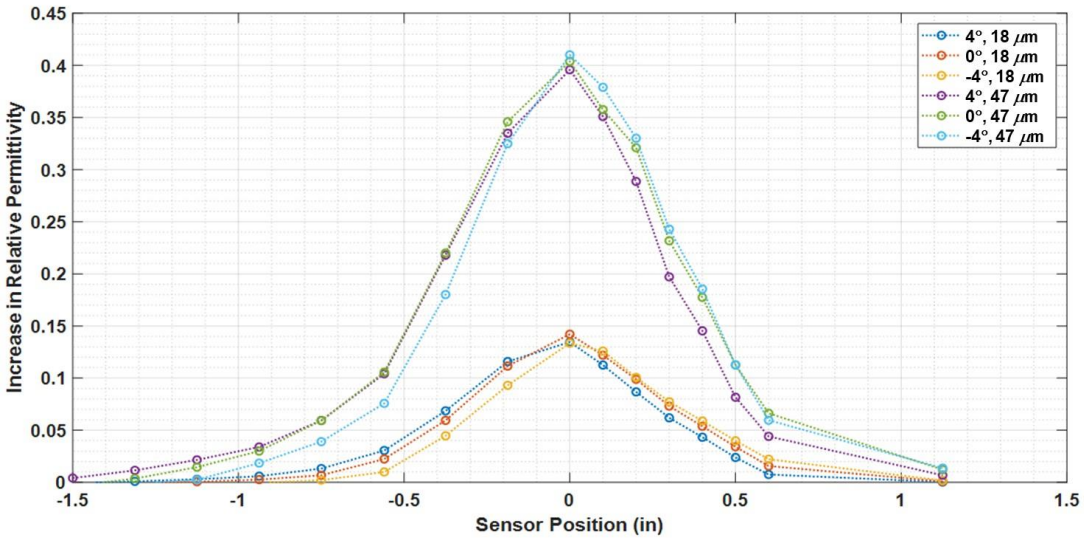

Figure 33. Angle of attack investigation using blotter cloth approach

Figure 34 presents the LEWICE predictions for the variations in collection efficiency for a 21-in NACA 0012 airfoil exposed to the AOA1 and AOA2 cloud conditions in Table 3. The simulation results reported in Figure 34 were performed using monodisperse droplet distributions instead of the seven-bin Langmuir-D distribution commonly used for IRT case predictions. Additionally, since the 47-μm case is near the lower limit of the Appendix O or SLD conditions, the 47-μm case was simulated with and without the splashing model. The LEWICE results of

Figure 34 do not exhibit a substantial difference with or without the splashing model for the 47-μm case. However, the lack of difference could be from either the low airspeeds used in the LFACT or the choice of a monodisperse model.

While the model used in the LFACT is not a complete 21-in model, the leading edge variations at 0°-AOA are expected to be essentially the same for the multi-waveguide sensor model. While Figure 33 and Figure 34 present two different things, increase in relative permittivity and surface collection efficiency, the trends in each curve and the relative changes between the two conditions at each location along the airfoil should be similar. In comparing the results shown in Figure 33 and Figure 34, two differences are 1) the surface variations of the collection efficiency do not decay as quickly in the direction of increasing distance from the leading edge as noted for the increase in relative permittivity and 2) the ratio of the leading edge permittivity between the two cases is larger than the ratio of the leading edge collection efficiencies for the LEWICE simulations. Cloud non-uniformity was suspected as the cause of the differences between the variations in the increase in relative permittivity and the surface collection efficiency.

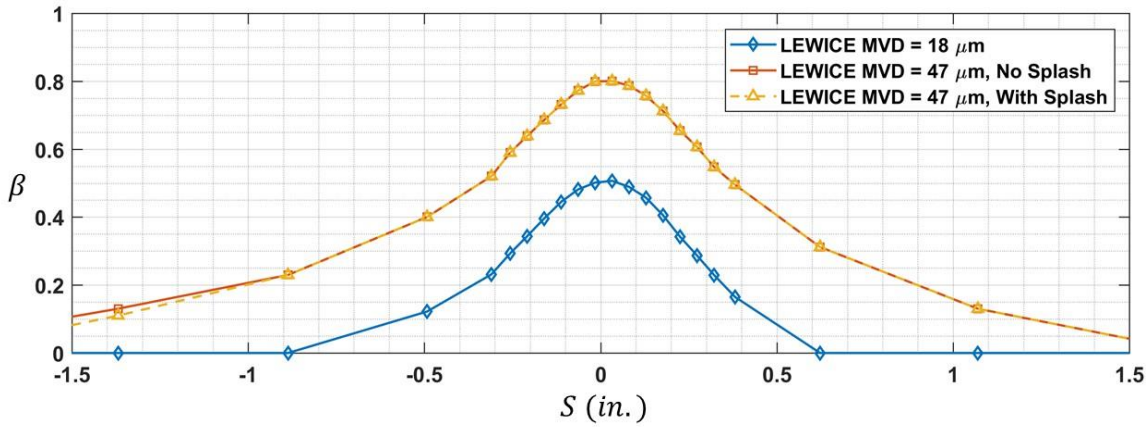

Figure 34. LEWICE prediction for collection efficiency variations on 21-in NACA 0012 at 0° AOA and 22 m/s

Shifting to the AOA variation results in Figure 33, the different model angles of attack produced subtle differences in the surface variations for each cloud condition. However, the differences were not as significant as expected based on LEWICE simulations for complete 21-in NACA 0012 model. Since the model was created using only the leading three inches from a 21-in NACA 0012 airfoil shape, the LFACT model did not produce the same flow circulation as a full 21-in model would have produced. Consequently, the flow and resulting surface collection efficiency variations did not change as much as expected for the truncated model used in the LFACT tests. The LFACT model employed for the multi-waveguide sensor was intended to be a component of a hybrid or multi-element model used to generate the same circulation without the

size of the full model (Fujiwara & Bragg, 2019). The implementation of the hybrid airfoil system is planned following the completion of the current research activities.

6.4.4 Fast multiplexing approach with blotter cloth

Following the AOA investigation using the multi-waveguide sensor, the speed of the acquisition process was improved significantly. While the results presented in Figure 33 demonstrated a high level of repeatability, if not the intended effects of the angle of attack, the effects of evaporation and the drying of the cloth following the end of a spray was noticed in the AOA cases. The increase in speed of acquisition was performed to reduce the effects of blotter-cloth drying between the end of a spray and the beginning of the multi-waveguide measurement sequence. Also, the sequence of the sensors was changed to measure the waveguides in order of surface distance from the leading edge instead of minimum S location to maximum S location. The multiplexing process to read all sixteen waveguides was reduced from 30 seconds to approximately 0.1 seconds.

To evaluate the new faster multiplexing approach to the blotter cloth measurements, a set of repeatability tests were performed using the Repeat1 and Repeat2 cloud conditions identified in Table 3. The repeatability tests consisted of exposing the multi-waveguide sensor to the Repeat1 and Repeat2 clouds for various exposure times.

The results of the repeatability investigation are presented in Figure 35. The vertical axis of Figure 35 is the increase in permittivity measured at each waveguide divided by mass of water released by the center nozzle of the spray bar system over the spray or exposure time of the test. Since the spray time is changing, dividing by the mass of water released for each spray enables a comparison of the change in relative permittivity per mass of water impinging the sensor region. Figure 35 demonstrates that when the spray time was varied, variations at each waveguide were present. These variations were suspected to have been caused by the repeatability in the cloud generation. However, in inspecting the six second case for the Repeat1 (52 μm) cloud, the variation in the increase in permittivity began to spread out from the leading edge region. This spreading was suspected as coming from seeping or spreading of the water through the cloth as substantially more water was impacting the multi-waveguide sensor model. However, even for the 15 second case for the Repeat2 (21 μm) cloud, the spreading was not as noticeable as for the six second case for the Repeat1 cloud. Thus, care must be taken when operating using the blotter-cloth approach so that water does not locally flood the blotter substance and begin to run-back along the model surface. For the Repeat1 (52 μm) cloud, the maximum exposure time was four seconds, while the Repeat2 cloud cases allowed exposures of over 10 seconds. The

difference in exposure limits for the two cases given the close LWC_D values reinforced suspicions of cloud non-uniformity with in the LFACT.

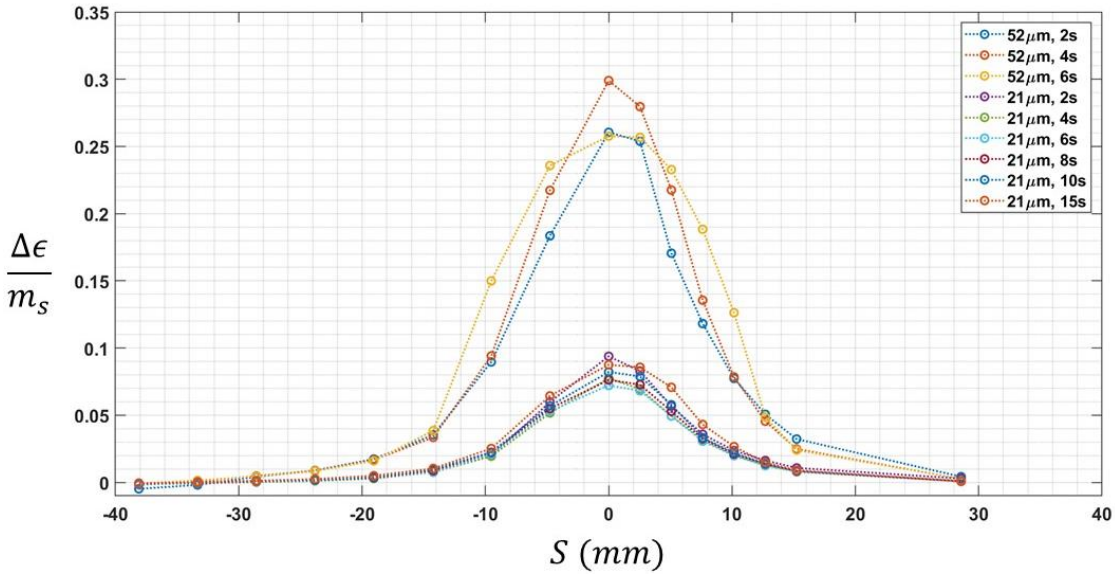

Figure 35. Repeatability results using fast multiplexing of waveguides

6.5 Multi-waveguide sensor measurement summary

The multi-waveguide sensor model was constructed and tested in three operating modes. The blotter-cloth approach was determined to be the most useful and most successful approach for using the sensors in LFACT testing and in potential use on larger icing wind tunnels such as the IRT. In the repeatability and AOA investigations, the waveguides responded as expected based on their locations from the leading edge of the model. The difference in the response of the waveguides to different cloud conditions and the difference in the response to different spray times were more significant than expected. However, the sources of the differences were thought to be caused by 1) the lack of uniformity of the cloud generated by the spray bar system, 2) the lack of consistent spray pressures and mass flow rates as a function of time, and 3) the time required to generate the correct cloud conditions. Because of the suspected causes of the differences, characterization of the cloud properties was crucial for the continued validation of the multi-waveguide sensor system.

7 Wind tunnel cloud validations

A WCM-2000 water content measuring system from SEA, Inc. (SEA Inc., 2016), was used to characterize the cloud variation within the LFACT. The WCM-2000 was also used to characterize the actuation time, or the amount of time required for the spray system to reach the

desired cloud properties. The WMC-2000, shown in Figure 36, was mounted on a two-dimensional positioning system as shown in Figure 36(b), at a location approximately 4 inches downstream of the location where the microwave sensors were mounted in the tunnel. Figure 36(a) presents a front view of the WCM-2000 sensing head, and Figure 36(c) demonstrates the sensing head and the sensor connection boom or mounting system.

7.1 Cloud uniformity characterization

For the cloud uniformity studies, the WCM-2000 sensing head was moved through the cross section of the LFACT in one-inch increments over the center 10 inches in the vertical (spanwise) direction and the center 10 inches in the flow-normal direction. At each measurement station, the WMC-2000 sampled the cloud for 3-5 seconds depending on the test. The WCM-2000 was used with sensing heads (SN 2016 and SN 2033). Each head was used to characterize the cloud uniformity for each of the conditions used for the AOA investigations for all sensors and for the repeatability cases for the multi-waveguide sensor.

Figure 37 presents the LWC cloud uniformity measurements for the AOA investigations with all sensors, and Figure 38 presents the LWC cloud uniformity measurements for the repeatability cases with the multi-waveguide sensor. In Figure 37 and Figure 38, the black lines show the position and blockage region of the sensors, and the red box indicates the sensing area of the multi-waveguide sensor.

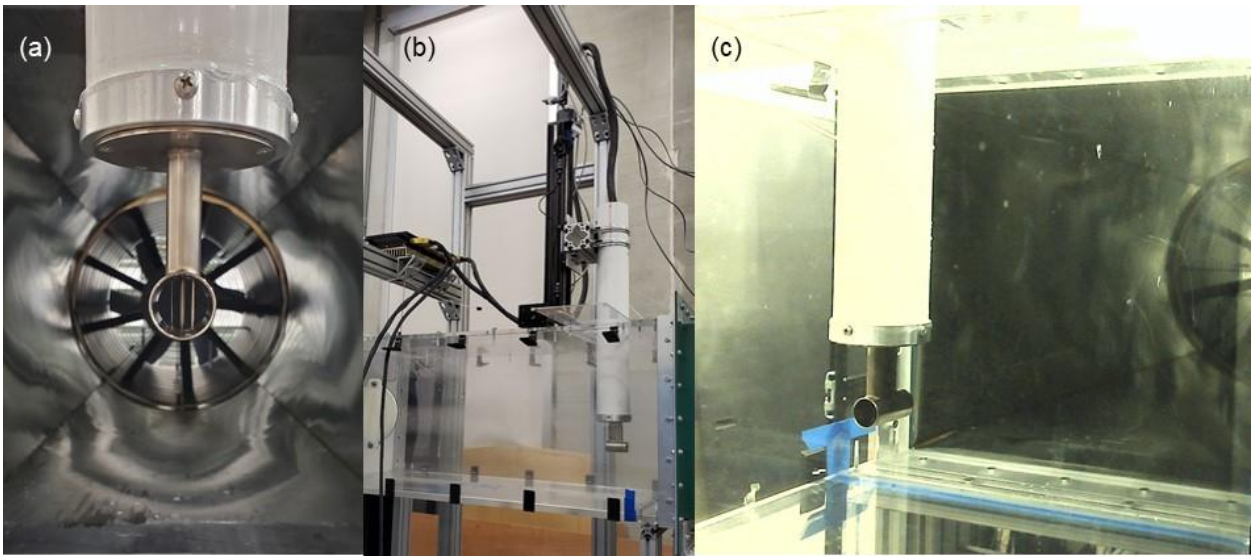

Figure 36. WCM-2000 installed and Operating in the LFACT
(a) Front view, (b) Side view during cloud measurement, and (c) Side view operating dry

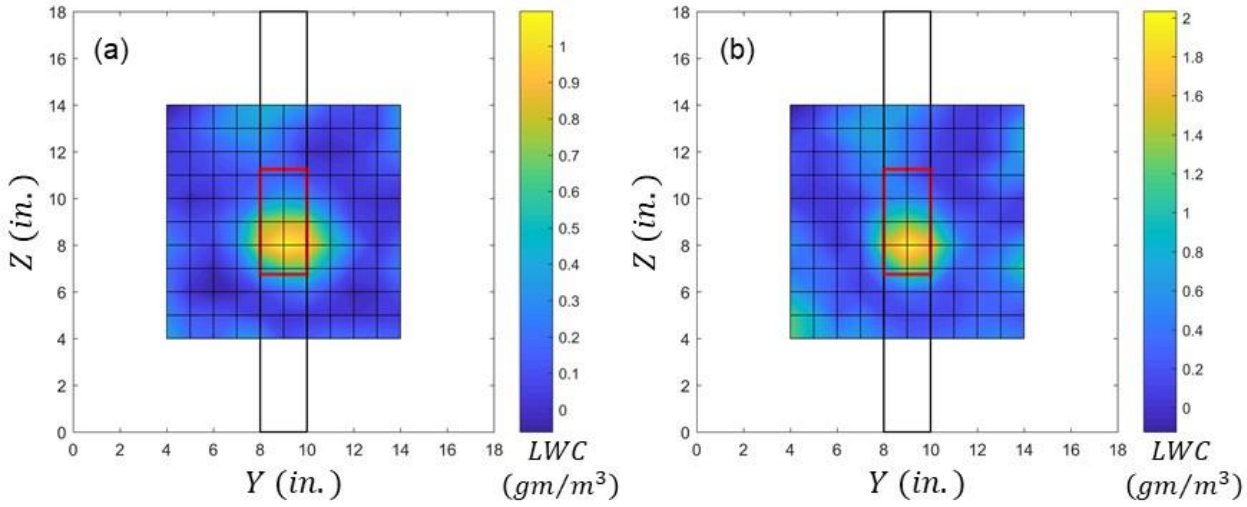

Figure 37. Cloud LWC variation generated for the AOA investigations for all sensors (a) P_{air} = 20 psi, P_{H2O} = 14.4 psi, MVD = 18 μm, AOA2 (b) P_{air} = 10 psi, P_{H2O} = 7.4 psi, MVD = 47 μm, AOA1

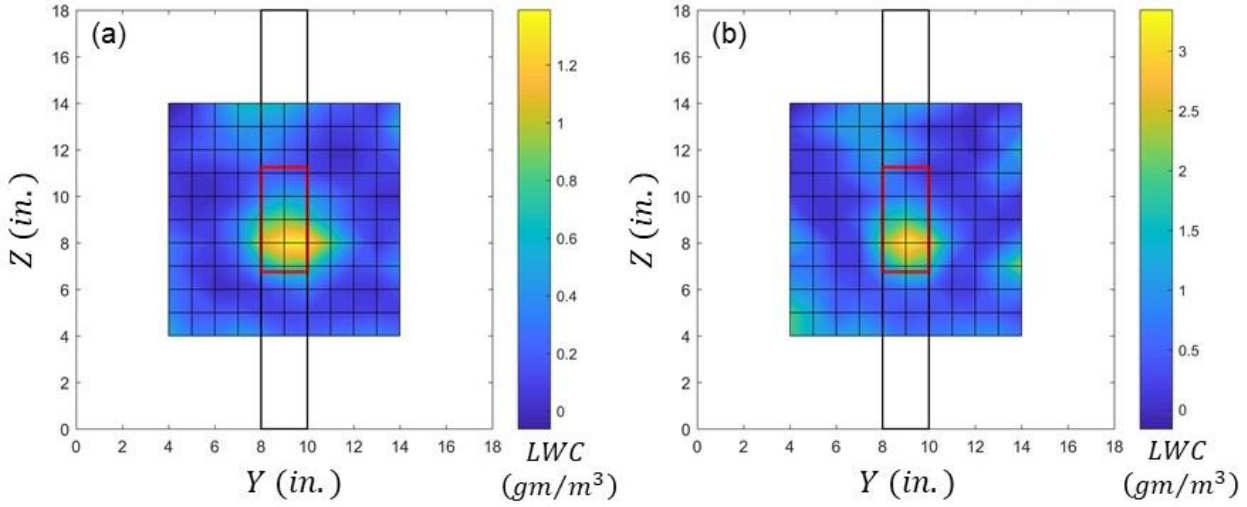

Figure 38. Cloud LWC variation generated for the multi-waveguide sensor repeatability study (a) P_{air} = 20 psi, P_{H2O} = 15.6 psi, MVD = 21 μm, and (b) P_{air} = 10 psi, P_{H2O} = 8.6 psi, MVD = 52 μm

Figure 37 and Figure 38 demonstrate that the clouds generated by the LFACT spray system were non-uniform. Over the sensing area of the multi-waveguide sensor, the cloud appears to exhibit a two-dimensional Gaussian distribution with a maximum LWC of 1.4 to 3 times the design LWCs identified in Table 2 and Table 3.

7.2 Cloud non-uniformity effects on sensor performance

The cloud non-uniformities captured in Figure 37 and Figure 38 explain many performance features of the single-waveguide and multi-waveguide sensors. Figure 39 presents the LEWICE

predictions from Figure 34 and the 0° AOA measurements for the multi-waveguide sensor presented in Figure 33. Since the AOA1 cloud (47 μm) was near Appendix O or SLD conditions, the LEWICE simulations were performed with and without the splashing model.

In Figure 39, the change in permittivity is scaled by the ratio of the design LWC values from Table 3 to the maximum LWC values observed in Figure 37 for the AOA1 and AOA2 cases. While the scaling on the second axis for the permittivity measurements was chosen to best match the collection efficiency predictions, the scaling demonstrates that the ratio of the maximum permittivity changes between the two cases matches the ratio of the LEWICE predicted maximum collection efficiencies.

Further, once the cases are scaled properly, the 18 μm measurements AOA2 track the spatial variations in the collection efficiency predictions from LEWICE. The 47 μm measurements AOA1 track well in the leading edge region, but the capture limits are much narrower or decay more abruptly than the LEWICE predictions outside of $|S|$ = 0.3 in. In revisiting Figure 37(b), the distribution of the AOA1 cloud appears to be a much narrower Gaussian distribution with a higher maximum LWC than for the AOA2 cloud (18 μm). Since the MVD for the AOA1 cloud is larger (47 μm) and the cloud is more compact, the droplets do not follow the flow around the model and impact a much smaller region than predicted in LEWICE, which assumes a uniform droplet distribution. The splashing of the droplets was also suspected of causing the difference between the AOA1 (47 μm) measurements and predictions outside the leading edge region. However, as shown in Figure 39, the difference between the LEWICE predictions with and without the splashing model are insignificant except for the region S < 1.0 in.

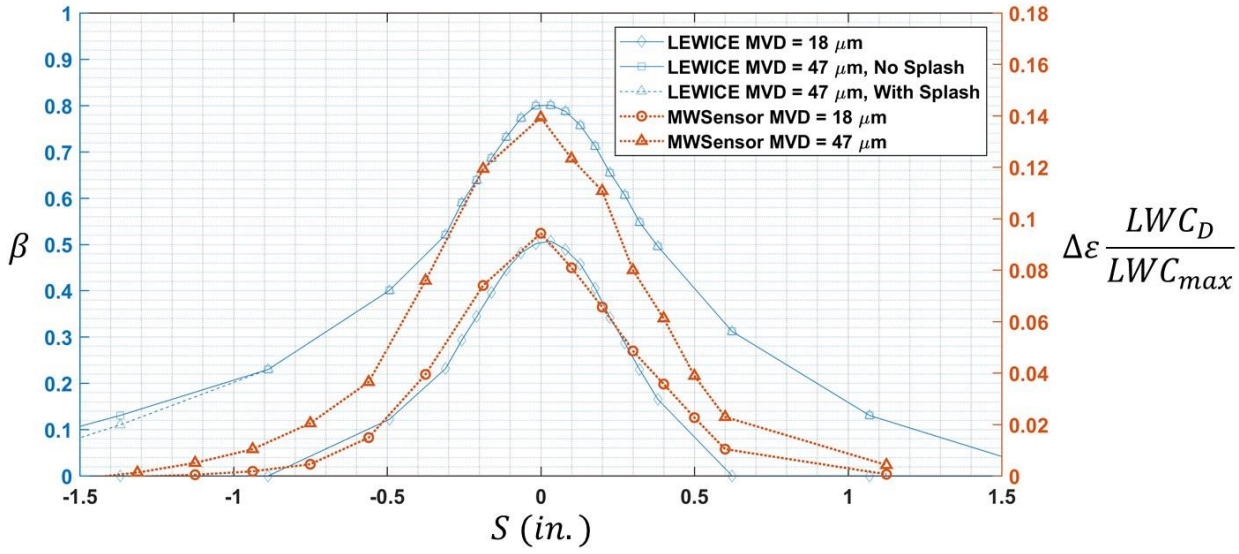

Figure 39. Comparison of collection efficiency simulations to permittivity increase measurements scaled by the maximum measured LWC for each cloud

7.3 Cloud actuation time

The second objective of the WCM-2000 measurements was to characterize the time required to create the desired cloud conditions following spray actuation. For the spray actuation investigation, the WCM-2000 probe head was placed at the station which exhibited the maximum LWCs in Figure 37 and Figure 38. For each cloud condition, the spray system was actuated while LWC measurements were being acquired from the WCM-2000.

Figure 40 presents the cloud transient measurements for the Repeat2 case from Table 3 when the spray is actuated with the turbine flowmeter bypass open and with the bypass closed, sequentially. Figure 40 demonstrates that the pneumatic actuation system establishes the cloud quickly. The desired properties of the cloud are reached within one second from cloud initiation when the flowmeter bypass is open. However, when the flowmeter is used during a test, the flow reaches the operating pressure within 4 seconds. While the response with the flowmeter bypass open was within one second, the response shown in Figure 40 includes the finite response time of the WCM-2000. Consequently, the actual cloud actuation time is shorter than one second when the flowmeter bypass is open.

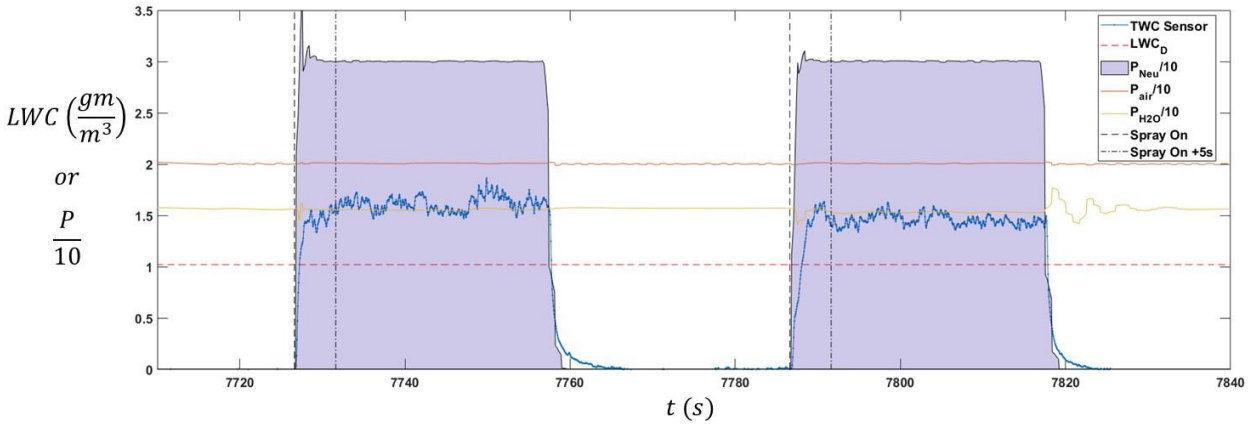

Figure 40. Transient response of WCM-2000 with flowmeter bypass open and without flowmeter bypass closed

While Figure 40 demonstrates that cloud actuation time is shorter than one second when the flowmeter bypass is open, sprays longer than five seconds are recommended. This result indicates that the lack of repeatability in the Sequential Direct Transient approach described in Section 6.4.1 was caused by cloud transient or start-up effects. That is, the Sequential Direct Transient measurements depended on the slope or rate of increase in permittivity to infer the initial rate of water accumulation at each waveguide, and the initial slope was calculated over the

same time (order of 1 second) over which Figure 40 indicates the flow was still being established.

The improved repeatability of the blotter-cloth measurements of Section 6.4.3 was achieved because those measurements were essentially a cumulative change in permittivity over a period longer than the transient or start-up time of the cloud. However, the upper limit on the spray time when using the blotter-cloth approach is the limit at which water floods the cloth and begins bleed or spread along the surface direction. Again, this effect was observed for the six second spray using Repeat1 (52 μm) cloud conditions in Figure 35.

8 Cloud non-uniformity and further validation efforts

Equation 1 for the definition of surface collection efficiency assumed a uniform cloud moving over a wing or airfoil model. Additionally, ice accretion solvers such as LEWICE include predictions based on the assumption of uniform distributions of the liquid water content. Figure 37 and Figure 38 demonstrate that the clouds generated in the LFACT are non-uniform at the airspeeds used in the current study.

The results depicted in Figure 39 are certainly encouraging, but the results shown indicate at best that the measurements of permittivity variations are proportional to the collection efficiency variations between the two cases in the stagnation region of the airfoils. Other than switching to a wind tunnel with demonstrated cloud uniformity to test the microwave sensors, methods must be identified to compare the microwave sensor performance to collection efficiency predictions from current and future ice-accretion prediction codes.

To further calibrate the single-waveguide and multi-waveguide sensors using LFACT tests, more advanced approaches to simulating the theoretical maximum collection along the surface are required. The options for proceeding are 1) to combine the uniform distribution simulations with the LWC map using a spatial convolution for a prediction of the impinging mass along the variation of the surface or 2) to perform simulations using non-uniform clouds passing through the LFACT test section. For both options, the validation efforts would switch from focusing on collection efficiency comparisons to comparisons of the mass of water or thickness of water captured on the surface and along each waveguide during a finite cloud exposure.

In the calibration of the multi-waveguide sensors shown in Figure 16, the average increase in sensor permittivity was related in terms of the volume of water added to the calibration area. If the volume of water were divided by the aperture area (the opening of the sensing region), the result would be a calibration of the increase in sensor permittivity to the average film thickness at

each waveguide. The two options for continued validation efforts are described in the following subsections in terms of an approach to predict the local thickness variations at each waveguide-surface distance location from the leading edge.

8.1 Convolution approach

When using simulations from clouds using a constant LWC value to compare to the measured water thickness at each wire, the predicted water thickness on the airfoil at the waveguide location are determined using Equation 9.

$$t_{w,P} = \frac{1}{(z_2 - z_1)(\Delta S)\rho_w} \int_{z_1}^{z_2} \int_{S-\frac{\Delta S}{2}}^{S+\frac{\Delta S}{2}} \beta_C(S)\, G_{LWC}(Y,Z)\, LWC_S\, V_\infty\, \Delta t_s\, dS dZ \tag{9}$$

In Equation 9, $\beta_C(S)$ is the collection efficiency from the simulation using a uniform LWC value and $G_{LWC}(Y,Z)$ is the spatial mapping of the relative water content as defined in Equation 10.

$$G_{LWC}(Y,Z) = \frac{LWC_M(Y,Z)}{LWC_S} \tag{10}$$

In Equation 10, $LWC_M(Y,Z)$ is a function that describes the measured LWC values in the cloud and LWC_S is the LWC value used in the simulations.

The most significant theoretical issues in implementing Equation 9 relate to the consistency of the MVD issues which would change the local collection efficiencies if the MVD varies spatially along the non-uniform cloud. The primary technical issues in employing Equation 9 are 1) the generation of the appropriate function for the cloud density description and 2) the mapping of the measured cloud density function from the spatial (*Y,Z*) coordinates back to the surface coordinates for the numerical integration. The usefulness and proper implementation for Equation 9 will be continued following the conclusion of the current research activities (McClain, Herrera, & Ahmed, 2022).

8.2 Non-uniform cloud simulations

The second option for future validation efforts using the non-uniform clouds in the LFACT is to employ computational simulations with spatial variations in cloud liquid water contents. Initial investigations have been performed using discrete-phase simulations using ANSYS/FLUENT. The most useful approach identified has been to employ group injections of non-interacting particles with a stagger radius to distribute the particles over a specified area. Figure 41 presents

an image of simulation results showing particle tracks from a group injection of 1000 particles with a 0.5-in stagger radius.

To replicate the non-uniformity of the LFACT clouds, the number of group injections and the number of particles within each group injection can be varied to represent the LWC distribution measured in the LFACT. The number of particles that terminate on each part of the surface can be determined from the particle tracks, and then the mass at each waveguide would be determined using Equation 11 based on a monodisperse droplet distribution.

$$t_{w,P} = \frac{1}{(z_2 - z_1)(\Delta S)\rho_w} \frac{\dot{m}_M}{\dot{m}_{Sim}} \sum_{z_2 - z_1} \left[N_C \, \frac{4}{3}\pi \left(\frac{MVD}{2} \right)^3 \right]_{S+\frac{\Delta S}{2}}^{S+\frac{\Delta S}{2}} \tag{11}$$

Initial simulations of non-uniform clouds have been performed as demonstrated by Figure 41. However, further simulations of non-uniform clouds and the investigations of the proper implementation of the approach will be required following the current research activities.

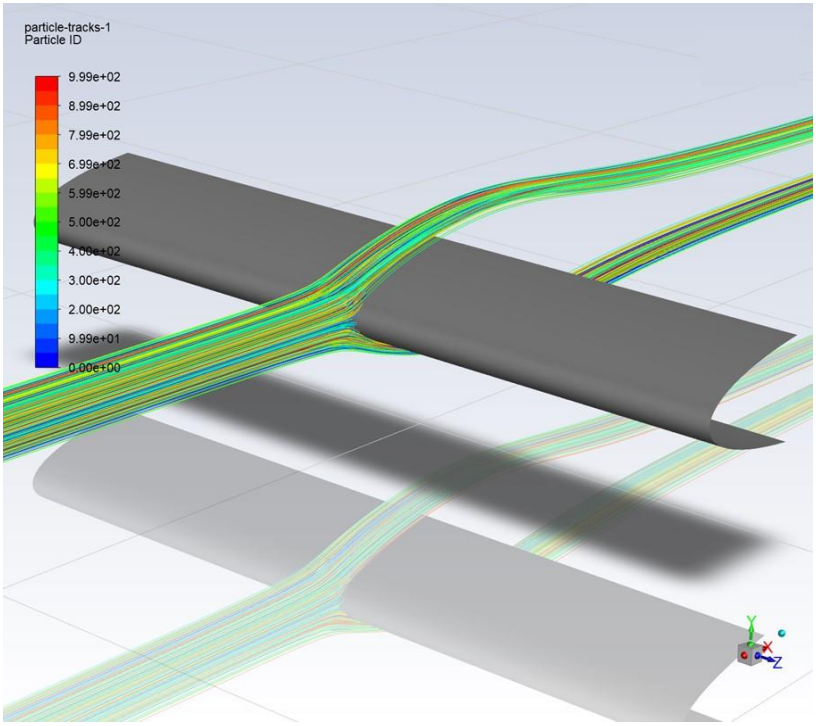

Figure 41. Simulation results showing particle tracks from a group injection with a 0.5-in radius for monodisperse, 21 μm Droplets, $V_\infty = 22\ m/s$

8.3 Continued validation efforts

The non-uniform clouds measured in the LFACT have created significant issues in the final calibrations of the sensors for collection efficiency measurements. Improvements to the spray system of the LFACT have been and will continue to be pursued. While improvements are pursued, additional resources are required to rent or purchase the WCM-2000 to quantify the improved LWC spatial variations and cloud response times if the spray system is altered in future efforts.

Because the cloud properties have been characterized for multiple operating conditions, research will continue using the current spray system. The known cloud condition variations will be accounted using either analytical or computational techniques. Progress has been made as part of the current research activities using both potential methods for compensating for the LFACT cloud uniformity. However, neither approach was fully implemented. Efforts on both approaches will continue following the conclusion of the current study.

9 Conclusions

Better measurements of surface collection efficiency of airfoils and airfoil components exposed to water clouds are required for the continued improvement of ice accretion codes used for the design certification of aircraft models. As part of the current research activities, a microwave sensing approach was developed to measure the water collecting on a wind tunnel model exposed to different cloud conditions. The microwave approach uses a vector network analyzer to characterize the phase delay of signals propagating along the wires over the range of 100 MHz to as high as 20 GHz. For the sensors with multiple waveguides, a multiplexing or switching system is required to measure the waveguide phase delay sequentially.

Three models were created for the study. Two models were created using single-waveguides for basic operational tests, and another multi-waveguide sensor was created to investigate water collection variations along the surface distance of a wind-tunnel airfoil leading-edge model. Each sensor model was created using flexible circuit boards glued to three-dimensionally printed models. An additional calibration apparatus was created using the same flexible circuit board and waveguide system as used for the multi-waveguide sensor.

A new spray system was also created for use in the LFACT. The spray system used a three-by-three array of air-assisted nozzles. The nozzles were pneumatically actuated for fast operation. Electronic regulators were used to control the water pressure, the air assist pressure, and the pneumatic actuation pressure to the nozzles.

The LFACT and spray system were used to test each sensor using different cloud conditions at 22 m/s, which was the limiting speed encountered using the Pi Sensor. The primary findings of the tests follow:

1) The operating principle and physics of the waveguide response to the presence of water was demonstrated using the single-waveguide models. The waveguides were sensitive to the accumulation of water during a cloud exposure. When exposed to a passing cloud, the permittivity increased asymptotically to a value determined by a steady-state film thickness. Based on the proof-of-concept measurements, a provisional patent (Application # 63/239,207) was filed for the flexible PCB and microwave sensing approach for liquid film thickness measurements with the title "A Microwave System for Detection and Characterization of Materials Interacting with Aircraft and Airfoil Surfaces."

2) The approach and sampling frequency range was identified using the single-waveguide sensors.

3) The repeatability and sensitivity of the single-waveguides to the model angle of attack was investigated. However, the repeatability and AOA sensitivity investigations were affected by the repeatability of the wind tunnel in establishing the clouds quickly compared to the linearity region of the sensors.

4) The multi-waveguide sensor and multiplexing system were demonstrated and refined. Through repeated tests, the total measurement time to characterize the permittivity change of all sixteen waveguides was reduced to approximately 0.1 seconds.

5) "Sequential Direct Transient" measurement approach was explored using the multi-waveguide sensor, and the approach focused on measuring the rate of permittivity increase at each waveguide individually. The Sequential Direct Transient approach was determined to be viable. However, the approach requires substantial time and may not be useful in large-scale icing wind tunnel tests because of the number of tests required to characterize the variations in collection efficiency along the surface distance of an airfoil model or wing. Additionally, the approach requires repeatable and precise generation (timing) of clouds to make comparisons of the collection rates between individual waveguides. In large icing wind tunnels, the repeatable and precise timing for cloud creation required may be difficult to achieve.

6) Steady-state film-thickness measurement approach was explored using the multi-waveguide sensor. Film dynamics and the shedding and run-back of the beads along the

model surface made the approach unreliable for inferred collection efficiency measurements.

7) The blotter cloth approach to characterizing the water collection was found to be the most repeatable when using the multi-waveguide sensor. The approach is like the approach of Papadakis et al. (2007) for collecting water on the surface of the airfoil, but the measurements are essentially immediate, and the cloth or paper can be reused between tests if sufficient time is provided for the paper or cloth to dry.

8) In addition to the theoretical predictions for permittivity change with the amount of water present, a calibration stand was used to develop a relationship between water thickness and the change in permittivity observed at each waveguide. The calibration was performed in direct mode and with the blotter cloth attached. The calibration procedure using the direct measurements (without the blotter cloth) were affected by the water pooling or forming large beads on the calibration surface.

9) A WCM-2000 was used to characterize the clouds generated in the LFACT. The clouds were shown to be non-uniform with variations in the LWC over the sensing regions of each sensor model. However, when the blotter cloth measurements were scaled using the measured LWC measurements, the ratio of the measured increases in permittivity between cases with different MVDs matched the ratio of predicted collection efficiency at the stagnation region of the sensor model. Additionally, the cloud start-up or initiation time was shown to be on the same order as the transient test timescale for the Sequential Direct Transient measurements.

Because of the cloud non-uniformity, two alternative approaches to validating the multi-waveguide sensor using the measured liquid water content variations were explored. Each approach will require inferences about collection efficiency based on the amount of mass or the thickness of water that collects at each waveguide location. Continued efforts following the completion of the current study will focus on 1) modification of collection efficiency predictions based on the measured cloud non-uniformity and 2) simulation of non-uniform clouds using multiple injections with different numbers of droplets. Improvements to the spray system of the LFACT will be pursued; however, additional resources will be required to rent or purchase the WCM-2000 to quantify the improved LWC spatial variations and cloud response times if the spray system is altered.

10 References

Aeronautics and space, airworthiness standards: transport category airplanes, 14 C.F.R. § 25, App. C. Retrieved from https://www.ecfr.gov/current/title-14/chapter-I/subchapter-C/part-25#Appendix-C-to-Part-25

Airplane and engine certification requirements in supercooled large drop, mixed phase, and ice crystal icing conditions, 79 Fed. Reg. 65507, (codified in 14 C.F.R. pts 25 and 33) (2015). Retrieved from https://rgl.faa.gov/Regulatory_and_Guidance_Library/rgNPRM.nsf/0/93f68c4985d8e796862577510060364f!OpenDocument&ExpandSection=-4

Fujiwara, G., & Bragg, M. (2019). Method for designing hybrid airfoils for icing wind-tunnel tests. *Journal of Aircraft, 56*(1), 137-149.

Hasted, J. (1973). *Aqueous dielectrics.* London: Chapman and Hall.

Langmuir, I., & Blodget, K. (1946). *A mathematical investigation of water droplet trajectories.* Army Air Forces Technical Report, No. 5418.

Levy, O., & Stroud, D. (1997). Maxwell Garnett theory for mixtures of anisotropic inclusions: Application to conducting polymers. *Physical Review B, 56*(13), 8035.

McClain, S., Herrera, B., & Ahmed, S. (2022). A microwave system for airfoil water collection efficiency measurements. *Submitted for the 2022 AIAA Aviation Forum and Exposition.* Chicago, IL.

Messinger, B. (1953). Equilibrium temperature of an unheated icing surface as a function of air speed. *Journal of the Aeronautical Sciences, 20*(1), 29-42.

Nyfors, E., & Vainikainen, P. (1989). *Industrial microwave sensors.* Norwood: Artech House.

Papadakis, M., Wong, S., Rachman, A., Hung, K., Vu, G. T., & Bidwell, C. (2007). *Large and small droplet impingement data on airfoils and two simulated ice shapes.* NASA/TM-2007-213959.

SEA Inc. (2016, June). *WCM-2000 Multi-Element water content system*. Retrieved from Science Engineering Associates, Inc., Products: http://www.scieng.com/products/multi.htm

Wright, W. (2008). *User's manual for LEWICE version 3.2.* NASA/CR-2008-214255.